

Using Silica Activity to Model Redox-dependent Fluid Compositions in Serpentinites from 100 to 700 °C and from 1 to 20 kbar

Codi Lazar  *

Department of Geological Sciences, California State University, San Bernardino, 5500 University Parkway, San Bernardino, CA, 92407, USA

*E-mail: clazar@csusb.edu

Received 23 March 2020; Accepted 9 October 2020

ABSTRACT

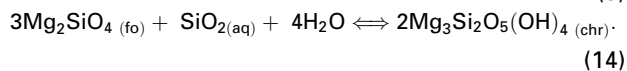
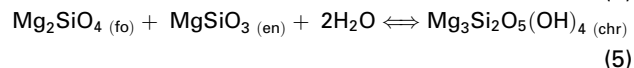
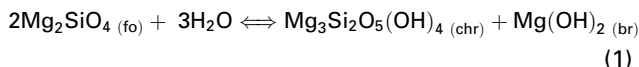
Serpentinization is a metamorphic process that can stabilize highly reduced hydrogen-rich fluids. Previous measurements of elevated CH₄ and H₂ concentrations in ultramafic-hosted submarine springs indicate that active serpentinization occurs along mid-ocean ridge systems at seafloor pressures (~<500 bar) and temperatures (~<350 °C). Serpentinites also exist at higher pressures in subduction zones; for example, during retrograde hydration of the forearc mantle wedge and during prograde deserpentinization within the subducted slab. However, many studies demonstrating the thermodynamic stability of reduced serpentine fluids have been limited to terrestrial seafloor conditions. To investigate the redox state of serpentine fluids at elevated pressures, phase equilibria and fluid compositions were computed for 100–700 °C and 1–20 kbar using aqueous silica activity ($a_{\text{SiO}_2(\text{aq})}$) as a governing parameter. Silica-sensitive, redox-buffering assemblages were selected to be consistent with previously proposed reactions: $\text{SiO}_2(\text{aq})$ –fayalite–magnetite (QFM), $\text{SiO}_2(\text{aq})$ –Fe-brucite–cronstedtite, $\text{SiO}_2(\text{aq})$ –Fe-brucite–Fe³⁺–serpentine, plus the silica-free buffer Fe-brucite–magnetite. Fluid species are limited to simple, zerovalent compounds. For silica-bearing redox reactions, $a_{\text{SiO}_2(\text{aq})}$ is buffered by coexisting ultramafic mineral assemblages in the system MgO–SiO₂–H₂O. Silica activity and f_{O_2} are directly correlated, with the most reduced fluids stabilized by the least siliceous assemblages. Silica activity and f_{O_2} increase with pressure, but are more strongly dependent on temperature, leading to greater silica enrichment and more oxidized conditions along shallow, warm subduction paths than along steeper, colder paths. Reduced fluids with $m_{\text{CH}_4}/m_{\text{CO}_2} > 1$ and f_{O_2} below QFM are present only when serpentine is stable, and are favored along all subduction trajectories except shallow P – T paths at eclogite-grade. Values of m_{H_2} and $m_{\text{CO}}/m_{\text{CO}_2}$ depend strongly on P and T , but also on the choice of redox buffer, especially whether the Fe-serpentine component is cronstedtite or Fe³⁺-serpentine. Methane and H₂S production are thermodynamically favored throughout the P – T range of the serpentinized forearc mantle and in other settings with similar conditions; for example, deep planetary seafloors. The model offers a generalized technique for estimating the redox state of a fluid-saturated serpentine at elevated P and T , and yields results consistent with previous petrographic and thermodynamic analyses. High-pressure serpentinization may be an important source of reduced species that could influence prebiotic chemistry, support microbial life in the deep biosphere or in deep planetary oceans, or promote greenhouse warming on early Earth.

Key words: serpentinization; forearc mantle wedge; abiotic methane; thermodynamic modeling; silica activity

INTRODUCTION

Reduced fluids in serpentinites

Serpentinization is a generalized term for retrograde metamorphism in ultramafic systems that produces one or more minerals in the serpentine group. It is possible to write a wide variety of stable reactions with a serpentine mineral as a product, but as a practical matter serpentinization is usually conceived as the destabilization of high-grade olivine-rich mantle rocks by aqueous fluids at lower metamorphic grades. In this respect, the most studied serpentinization reactions involve olivine and/or other ultramafic minerals (Table 1) reacting with H₂O to form a serpentine mineral such as lizardite, antigorite, or chrysotile. Several such reactions are listed in Table 2, for example:



Of particular interest to geochemists is the propensity of certain serpentinite assemblages to stabilize aqueous fluids with intensive properties unique among common hydrothermal systems. For example, artesian springs emerging from serpentinite-hosted aquifers contain waters with pH values up to 12.0, as highly alkaline as have been discovered in any natural aqueous fluid on Earth (Barnes & O'Neil, 1969; Barnes *et al.*, 1978). Another unusual feature of serpentinization is the production of fluids with remarkably low oxygen fugacity ($f\text{O}_2$) (Frost, 1985) and correspondingly high activities of reduced species such as H₂ and CH₄ (Shock, 1990; Sleep *et al.*, 2004). This property has gained much attention from the astrobiological community, where many researchers have proposed abiogenic serpentinization-derived organic compounds as building blocks for prebiotic chemicals, and as food and energy sources for primitive chemolithoautotrophic organisms hypothesized to exist within Earth's earliest ecosystems and on extraterrestrial bodies (Shock, 1990; Schulte *et al.*, 2006; Martin *et al.*, 2008; Sleep *et al.*, 2011).

Field evidence for reduced serpentinite fluids includes H₂ and CH₄ observed in submarine hydrothermal systems along the mid-Atlantic ridge system (Charlou *et al.*, 2002; Proskurowski *et al.*, 2008; Konn *et al.*, 2009), in terrestrial springs (Etiope *et al.*, 2011), and in olivine-hosted fluid inclusions (Klein *et al.*, 2019). Petrographic evidence for reducing conditions in serpentinites has been documented in the form of transition metal alloys and sulfides, common as accessory minerals in serpentinites (Dick, 1974; Frost, 1985; Lorand, 1988; Horita & Berndt, 1999; Klein & Bach, 2009). Such alloys include awaruite (Ni₃Fe) and wairuite (Co₃Fe), both of which contain substantial native iron,

Table 1: Chemical compositions and abbreviations.

Mineral or species	Formula	Abbreviation
anthophyllite	Mg ₇ Si ₆ O ₂₂ (OH) ₂	anth
antigorite	Mg ₄₈ Si ₃₄ O ₈₅ (OH) ₆₂	atg
aqueous silica	SiO _{2(aq)}	SiO _{2(aq)}
brucite	Mg(OH) ₂	br
chrysotile/lizardite	Mg ₃ Si ₂ O ₅ (OH) ₄	chr/liz
cronstedtite	(Fe ₂ ⁺ Fe ³⁺)(Fe ³⁺ Si)O ₅ (OH) ₄	crn
enstatite	MgSiO ₃	en
fayalite	Fe ₂ SiO ₄	fa
Fe-brucite	Fe(OH) ₂	fbr
Fe ³⁺ -serpentine	Fe ³⁺ Si ₂ O ₅ (OH) ₄	fsrp
forsterite	Mg ₂ SiO ₄	fo
magnetite	Fe ₃ O ₄	mt
olivine	(Mg, Fe) ₂ SiO ₄	ol
talc	Mg ₃ Si ₄ O ₁₀ (OH) ₂	tc
quartz	SiO _{2(q)}	qz
water	H ₂ O	w

requiring very low $f\text{O}_2$ values approaching the iron-magnetite buffer (Frost, 1985). Sulfides include heazlewoodite (Ni₃S₂), a reduced sulfide known only in serpentinites. These accessory minerals have been documented in serpentinites representing a wide range of tectonic settings: extant hydrothermal systems in mid-ocean ridge systems (Klein *et al.*, 2019), obducted ophiolitic serpentinites (Dick, 1974; Schwarzenbach *et al.*, 2016), an island arc root (Gerlach *et al.*, 1981; Leeman *et al.*, 1995; Evans *et al.*, 2009), a forearc mantle diapir (Coleman, 1986), supra-subduction ophiolites (Evans *et al.*, 2017) and prograde alpine serpentinites (Peretti *et al.*, 1992).

Many studies have proposed theoretical frameworks for explaining the reduced conditions found in serpentinites. In a classic paper, Frost (1985) used phase equilibria in $f\text{O}_2$ -temperature space to suggest that serpentinites are redox-buffered by major metamorphic assemblages. Similar phase assemblage arguments have since been used to explain the association of serpentinites with hydrogen-rich fluids (Sleep *et al.*, 2004) and to correlate redox conditions to silica activity (Frost & Beard, 2007). Evans (2008) proposed that $f\text{O}_2$ is governed by iron partitioning among olivine, orthopyroxene, and serpentine. Other researchers have used reaction path modeling to simulate progressive serpentinization of selected bulk composition (Palandri & Reed, 2004; McCollom & Bach, 2009; Klein *et al.*, 2013).

All the above thermodynamic studies of serpentinization are valid for pressures less than 2 kbar, relevant to seafloor systems, ophiolites, and the very shallow crust (Palandri & Reed, 2004; Sleep *et al.*, 2004; Klein & Bach, 2009). However, serpentinization is not limited to low pressure (P). Experiments have demonstrated that serpentine-bearing assemblages are stable up to ~80 kbar (Ulmer & Trommsdorff, 1995). Seismic studies and thermal modeling suggest that serpentinization occurs at high P throughout the mantle wedge (Bostock *et al.*, 2002; Hyndman & Peacock, 2003). Serpentinites are also found in association with blueschist- and

Table 2: Equilibria adopted in the present study*Equilibria in the system MgO–SiO₂–H₂O*

(1)	fo–chr–br–H ₂ O	$2\text{Mg}_2\text{SiO}_4 + 3\text{H}_2\text{O} \rightleftharpoons \text{Mg}_3\text{Si}_2\text{O}_5(\text{OH})_4 + \text{Mg}(\text{OH})_2$
(2)	fo–atg–br–H ₂ O (I _A) [*]	$34\text{Mg}_2\text{SiO}_4 + 51\text{H}_2\text{O} \rightleftharpoons 20\text{Mg}(\text{OH})_2 + \text{Mg}_{48}\text{Si}_{34}\text{O}_{85}(\text{OH})_{62}$
(3)	fo–tc–atg–H ₂ O (I _B)	$4\text{Mg}_3\text{Si}_4\text{O}_{10}(\text{OH})_2 + 18\text{Mg}_2\text{SiO}_4 + 27\text{H}_2\text{O} \rightleftharpoons \text{Mg}_{48}\text{Si}_{34}\text{O}_{85}(\text{OH})_{62}$
(4)	fo–anth–tc–H ₂ O (I _C)	$5\text{Mg}_7\text{Si}_8\text{O}_{22}(\text{OH})_2 + 4\text{H}_2\text{O} \rightleftharpoons 9\text{Mg}_3\text{Si}_4\text{O}_{10}(\text{OH})_2 + 4\text{Mg}_2\text{SiO}_4$
(5)	fo–en–chr–H ₂ O	$\text{Mg}_2\text{SiO}_4 + \text{MgSiO}_3 + 2\text{H}_2\text{O} \rightleftharpoons \text{Mg}_3\text{Si}_2\text{O}_5(\text{OH})_4$
(6)	fo–en–atg–H ₂ O (I _D)	$14\text{Mg}_2\text{SiO}_4 + 20\text{MgSiO}_3 + 31\text{H}_2\text{O} \rightleftharpoons \text{Mg}_{48}\text{Si}_{34}\text{O}_{85}(\text{OH})_{62}$
(7)	fo–en–tc–H ₂ O (I _E)	$5\text{MgSiO}_3 + \text{H}_2\text{O} \rightleftharpoons \text{Mg}_3\text{Si}_4\text{O}_{10}(\text{OH})_2 + \text{Mg}_2\text{SiO}_4$
(8)	fo–en–anth–H ₂ O	$9\text{MgSiO}_3 + \text{H}_2\text{O} \rightleftharpoons \text{Mg}_7\text{Si}_8\text{O}_{22}(\text{OH})_2 + \text{Mg}_2\text{SiO}_4$
(9)	en–tc–atg–H ₂ O	$90\text{MgSiO}_3 + 45\text{H}_2\text{O} \rightleftharpoons \text{Mg}_{48}\text{Si}_{34}\text{O}_{85}(\text{OH})_{62} + 14\text{Mg}_3\text{Si}_4\text{O}_{10}(\text{OH})_2$
(10)	qz–anth–tc–H ₂ O	$3\text{Mg}_7\text{Si}_8\text{O}_{22}(\text{OH})_2 + 4\text{SiO}_{2(\text{aq})} + 4\text{H}_2\text{O} \rightleftharpoons 7\text{Mg}_3\text{Si}_4\text{O}_{10}(\text{OH})_2$
(11)	qz–en–anth–H ₂ O	$7\text{MgSiO}_3 + \text{SiO}_{2(\text{aq})} + \text{H}_2\text{O} \rightleftharpoons \text{Mg}_7\text{Si}_8\text{O}_{22}(\text{OH})_2$
(12)	br–atg–fluid [†]	$48\text{Mg}(\text{OH})_2 + 34\text{SiO}_{2(\text{aq})} \rightleftharpoons \text{Mg}_{48}\text{Si}_{34}\text{O}_{85}(\text{OH})_{62} + 17\text{H}_2\text{O}$
(13)	fo–br–fluid	$2\text{Mg}(\text{OH})_2 + \text{SiO}_{2(\text{aq})} \rightleftharpoons \text{Mg}_2\text{SiO}_4 + 2\text{H}_2\text{O}$
(14)	fo–chr–fluid	$3\text{Mg}_2\text{SiO}_4 + \text{SiO}_{2(\text{aq})} + 4\text{H}_2\text{O} \rightleftharpoons 2\text{Mg}_3\text{Si}_2\text{O}_5(\text{OH})_4$
(15)	fo–atg–fluid	$24\text{Mg}_2\text{SiO}_4 + 10\text{SiO}_{2(\text{aq})} + 31\text{H}_2\text{O} \rightleftharpoons \text{Mg}_{48}\text{Si}_{34}\text{O}_{85}(\text{OH})_{62}$
(16)	fo–tc–fluid	$3\text{Mg}_2\text{SiO}_4 + 5\text{SiO}_{2(\text{aq})} + 2\text{H}_2\text{O} \rightleftharpoons 2\text{Mg}_3\text{Si}_4\text{O}_{10}(\text{OH})_2$
(17)	fo–anth–fluid	$7\text{Mg}_2\text{SiO}_4 + 9\text{SiO}_{2(\text{aq})} + 2\text{H}_2\text{O} \rightleftharpoons 2\text{Mg}_7\text{Si}_8\text{O}_{22}(\text{OH})_2$
(18)	atg–talc–fluid	$\text{Mg}_{48}\text{Si}_{34}\text{O}_{85}(\text{OH})_{62} + 30\text{SiO}_{2(\text{aq})} \rightleftharpoons 16\text{Mg}_3\text{Si}_4\text{O}_{10}(\text{OH})_2 + 15\text{H}_2\text{O}$
(19)	atg–en–fluid	$\text{Mg}_{48}\text{Si}_{34}\text{O}_{85}(\text{OH})_{62} + 14\text{SiO}_{2(\text{aq})} \rightleftharpoons 48\text{MgSiO}_3 + 31\text{H}_2\text{O}$
(20)	tc–anth–fluid	$3\text{Mg}_7\text{Si}_8\text{O}_{22}(\text{OH})_2 + 4\text{SiO}_{2(\text{aq})} + 4\text{H}_2\text{O} \rightleftharpoons 7\text{Mg}_3\text{Si}_4\text{O}_{10}(\text{OH})_2$
(21)	tc–en–fluid	$3\text{MgSiO}_3 + \text{SiO}_{2(\text{aq})} + \text{H}_2\text{O} \rightleftharpoons \text{Mg}_3\text{Si}_4\text{O}_{10}(\text{OH})_2$
(22)	fo–atg–br–SiO _{2(aq)}	$17\text{Mg}_2\text{SiO}_4 + 62\text{Mg}(\text{OH})_2 + 51\text{SiO}_{2(\text{aq})} \rightleftharpoons 2\text{Mg}_{48}\text{Si}_{34}\text{O}_{85}(\text{OH})_{62}$
(23)	fo–en–SiO _{2(aq)}	$\text{Mg}_2\text{SiO}_4 + \text{SiO}_{2(\text{aq})} \rightleftharpoons 2\text{MgSiO}_3$
(24)	en–anth–tc	$\text{Mg}_3\text{Si}_4\text{O}_{10}(\text{OH})_2 + 4\text{MgSiO}_3 \rightleftharpoons \text{Mg}_7\text{Si}_8\text{O}_{22}(\text{OH})_2$
<i>Redox equilibria</i>		
(25)	qz–fa–mt ‘QFM’	$2\text{Fe}_3\text{O}_4(\text{mt}) + 3\text{SiO}_{2(\text{qz})} \rightleftharpoons 3\text{Fe}_2\text{SiO}_4(\text{fa}) + \text{O}_{2(\text{g})}$
(26)	fluid–fa–mt ‘SFM’	$2\text{Fe}_3\text{O}_4(\text{mt}) + 3\text{SiO}_{2(\text{aq})} \rightleftharpoons 3\text{Fe}_2\text{SiO}_4(\text{fa}) + \text{O}_{2(\text{g})}$
(27)	fluid–fbr–crn ‘SBC’	$2(\text{Fe}^{2+}\text{Fe}^{3+})(\text{Fe}^{3+}\text{Si})\text{O}_5(\text{OH})_4(\text{crn}) + 4\text{H}_2\text{O} \rightleftharpoons 8\text{Fe}(\text{OH})_{2(\text{fbr})} + 2\text{SiO}_{2(\text{aq})} + \text{O}_{2(\text{g})}$
(28)	fluid–fbr–fsrp ‘SBS’	$2\text{Fe}_2^{3+}\text{Si}_2\text{O}_5(\text{OH})_{4(\text{fsrp})} \rightleftharpoons 4\text{Fe}(\text{OH})_{2(\text{fbr})} + 4\text{SiO}_{2(\text{aq})} + \text{O}_{2(\text{g})}$
(29)	fluid–fbr–mt ‘FBM’	$6\text{Fe}(\text{OH})_{2(\text{fbr})} + \text{O}_{2(\text{g})} \rightleftharpoons 2\text{Fe}_3\text{O}_4(\text{mt}) + 6\text{H}_2\text{O}$
(30)	H ₂ O–H ₂	$2\text{H}_2\text{O} \rightleftharpoons 2\text{H}_{2(\text{aq})} + \text{O}_{2(\text{g})}$
(31)	CH ₄ –CO ₂	$4\text{H}_{2(\text{aq})} + \text{CO}_{2(\text{aq})} \rightleftharpoons 2\text{H}_2\text{O} + \text{CH}_{4(\text{aq})}$
(32)	CO–CO ₂	$2\text{CO}_{2(\text{aq})} \rightleftharpoons 2\text{CO}_{(\text{aq})} + \text{O}_{2(\text{g})}$
(33)	H ₂ S–SO ₂	$2\text{SO}_{2(\text{aq})} + 2\text{H}_2\text{O} \rightleftharpoons 2\text{H}_2\text{S}_{(\text{aq})} + \text{O}_{2(\text{g})}$

^{*}I_n corresponds to invariant points shown in Fig. 4.

[†]Fluid refers to an SiO₂-bearing aqueous solution.

eclogite-grade lithologies exhumed from subduction zones (Brown *et al.*, 1982; Fryer *et al.*, 1999; Tsujimori *et al.*, 2007; Evans *et al.*, 2017). Moreover, reports of awaruite in high-pressure serpentinites suggest that the strongly reduced fluids associated with serpentinization also occur in rocks at great depths; for example, in the New Idria serpentinite forearc diapir in central California (Coleman, 1986; Murrey & Lazar, 2019) inferred to form at $P > 15$ –20 kbar (Tsujimori *et al.*, 2007; Yamada *et al.*, 2019), in the New Caledonia supra-subduction mantle at P up to 18 kbar (Evans *et al.*, 2017), and in prograde deserpentinized metaperidotites in the Malenco Peridotite, Italy, at P up to 4.5 kbar (Peretti *et al.* 1992).

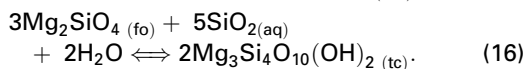
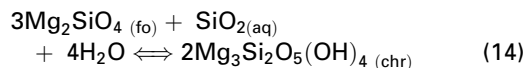
Thermodynamic investigations of serpentinization at subduction pressures have been improved by the recent development of the Deep Earth Water (DEW) model (Sverjensky *et al.*, 2014), which combines new estimates of the dielectric constant of H₂O to 60 kbar and 1200 °C with an abundant literature of experimentally determined mineral solubilities at high pressures (e.g. Dolejš & Manning, 2010). Debret & Sverjensky (2017) applied the DEW model to conclude that prograde deserpentinization in the subducted slab yields oxidized fluids at 630–660 °C and 20 kbar. Piccoli *et al.* (2019) predicted the release of reduced fluids from the

slab at higher grade sub-arc conditions during chlorite breakdown at and above ~770 °C and ~30 kbar.

Continuing in the spirit of this recent trend in the thermodynamic modeling of fluid–rock interactions at high-pressure conditions, this study applies the DEW model to survey the effects of pressure on redox-dependent fluid compositions equilibrated during serpentinization and related hydrous ultramafic reactions at 1–20 kbar and 100–700 °C. The results may be useful for modeling redox processes in subduction zones, deep planetary seafloors, and any other high-pressure setting in which serpentinization may occur. The unifying parameter of the present calculations is aqueous silica activity ($a_{\text{SiO}_{2(\text{aq})}}$), building on the work of Frost & Beard (2007). Other parameters and approaches are available to investigate the chemistry of serpentinite fluids, including iron partitioning, bulk-rock composition, disequilibrium processes, open-system processes, and more. However, as Frost & Beard (2007) pointed out, the unusually low silica activity in serpentinites is a useful framework for explaining the unusually low f_{O_2} values commonly associated with these rocks. Moreover, silica activity is expected to be sensitive to pressure, as implied by the strong dependence of quartz solubility on pressure (Dolejš & Manning, 2010).

A brief review of the link between silica activity and fO_2 in serpentinites

The relationship between fO_2 and $aSiO_{2(aq)}$ is briefly illustrated below by a thermodynamic analysis of the following two ultramafic metamorphic reactions in the system MgO–SiO₂–H₂O:



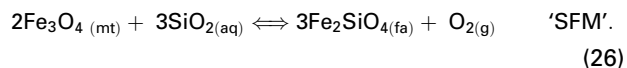
Assuming pure Mg-chrysotile and Mg-talc, and that $aH_2O = 1$, equilibrium expressions for reactions (14) and (16) may be written algebraically as

$$\text{forsterite–chrysotile : } \log aSiO_{2(aq)} = \log K_{14} - 3 \log X_{fo} \quad (34)$$

$$\text{forsterite–talc : } \log aSiO_{2(aq)} = 1/5 [\log K_{16} - 3 \log X_{fo}] \quad (35)$$

where olivine is assumed to be an ideal solution with a composition of Fo₉₀, a canonically representative mantle value. Equations (34) and (35) were computed for $P = 1$ kbar and plotted as $\log aSiO_{2(aq)}$ versus temperature (T) over the range 350–500 °C (Fig. 1a). These two univariant reactions intersect at a forsterite–chrysotile–talc–fluid invariant point at ~430 °C. The other univariant reactions that radiate from this point are omitted to focus solely on the effect of $aSiO_{2(aq)}$ on reactions (14) and (16). Figure 1a illustrates the dependence of silica activity on the identity of the stable assemblage. The fo–chr–fluid assemblage buffers $aSiO_{2(aq)}$ to lower values than does the fo–tc–fluid assemblage, a property that parallels the silicon content of the mineral formulae; for example, the Si–Mg ratio in chrysotile is <1 and the Si–Mg ratio in talc is >1.

Connecting $aSiO_{2(aq)}$ to fO_2 is allowed by two simultaneous equilibria involving the forsterite and fayalite components in the olivine solid solution series. Silica activity is buffered by equilibrium with the forsterite component of olivine in the system MgO–SiO₂–H₂O, as described above. Oxygen fugacity is buffered by equilibrium with the fayalite component of olivine in the system FeO–SiO₂–O₂. A classic redox reaction involving olivine is the quartz–fayalite–magnetite buffer [QFM; reaction (25)], and an analogous equilibrium may be written between aqueous silica, fayalite, and magnetite (SFM):



This formulation adopts an aqueous standard state for SiO₂ that is physically appropriate for serpentinites, given that the stable coexistence of quartz in ultramafic bulk compositions is forbidden. Combination of reactions (14), (16), and (26) implies the stable coexistence of olivine, serpentine, and magnetite, an assemblage that has been observed in prograde serpentinites

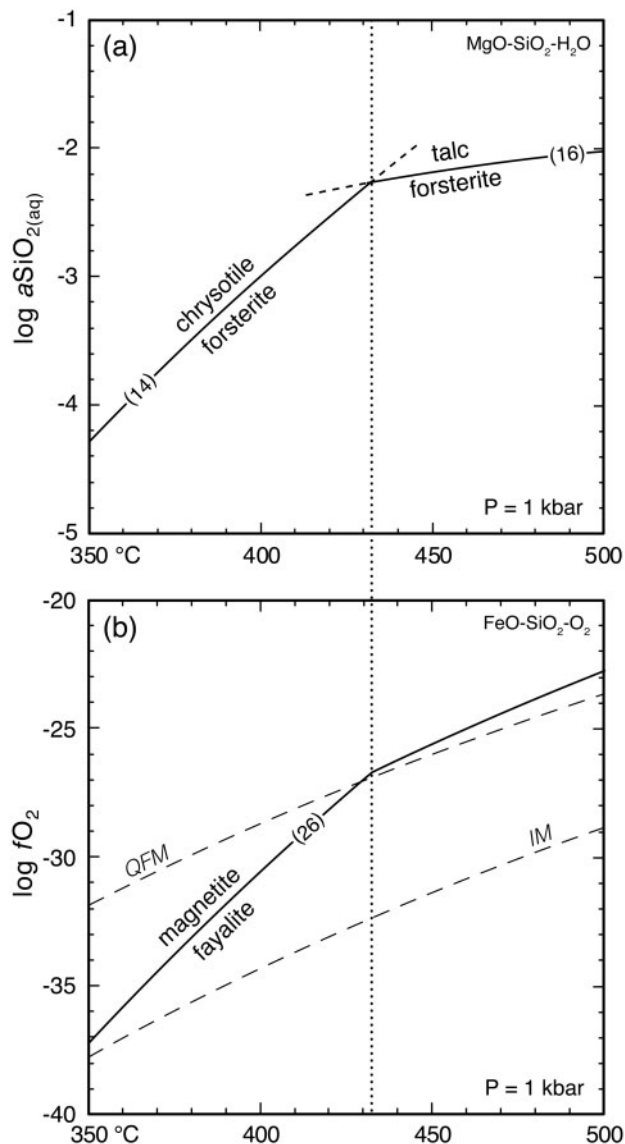


Fig. 1. The direct relationship between $aSiO_{2(aq)}$ and fO_2 for selected olivine–magnetite equilibria at $P = 1$ kbar, 350–500 °C, and $aH_2O = 1$. (a) Silica activity buffered by forsterite–chrysotile [reaction (14)] and forsterite–talc [reaction (16)] in the system MgO–SiO₂–H₂O. Metastable extensions are shown by dashed lines, which intersect at the chrysotile–talc–forsterite–H₂O invariant point. (b) fO_2 values for the silica–fayalite–magnetite (SFM) redox buffer [reaction (26)] in the system FeO–SiO₂–O₂ with $aSiO_{2(aq)}$ fixed by the reactions in (a). X_{fa} in olivine = 0.1. The vertical dotted line is a graphic connection between the two plots, highlighting the coincidence of the phase transition in (a) with the fO_2 slope change in (b). Dashed lines in (b) denote the fO_2 buffers QFM and IM.

(Peretti *et al.*, 1992; Khedr & Arai, 2012; Piccoli *et al.*, 2019). Several previous studies suggested that the stable coexistence of olivine and magnetite is rare during retrograde serpentinization (e.g. in abyssal peridotites). In these cases, other silica-dependent redox reactions may be more appropriate; for example, between ferrous brucite and Fe³⁺-serpentine (Klein *et al.*, 2009, 2013; McCollom & Bach, 2009; Tutolo *et al.*, 2020). Such equilibria will be considered in subsequent sections.

Table 3: Thermodynamic parameters for selected Fe-bearing minerals

Mineral	$\Delta_a G^\circ$ (kJ mol ⁻¹)	a	b ($\times 10^3$)	c ($\times 10^{-5}$)	S° (J mol ⁻¹ K ⁻¹)	V° (cm ³ mol ⁻¹)
cronstedtite ¹	-2613.45	354.76	175.06	-52.20	307.52	110.90
Fe-brucite ²	-486.98	116.06	8.65	-2.87	87.90	26.43
Fe ³⁺ -serpentine ³	-2963.78	287.73	188.20	-69.83	228.11	105.03

a , b and c are Maier–Kelly coefficients with units of J mol⁻¹ K⁻¹, J mol⁻¹ K⁻², J K mol⁻¹, respectively.

¹Values for a , b , c , S° and V° are from the slop98.dat SUPCRT database; $\Delta_a G^\circ$ is from Wolery & Jove-Colon (2004).

²Wolery & Jove-Colon (2004).

³Klein *et al.* (2009).

Assuming pure magnetite, and continuing with the assumption that olivine is an ideal solution, reaction (26) may be written as the following equilibrium expressions:

$$K_{\text{SFM}} = X_{\text{fa}}^3 f_{\text{O}_2} a_{\text{SiO}_2}^3 \quad (36)$$

or

$$\log f_{\text{O}_2} = \log K_{\text{SFM}} + 3 \log a_{\text{SiO}_2(\text{aq})} - 3 \log X_{\text{fa}}. \quad (37)$$

These expressions show that, at constant X_{fa} , silica activity and oxygen fugacity are directly correlated: an increase in $a_{\text{SiO}_2(\text{aq})}$ must result in an increase in f_{O_2} , and vice versa. Oxygen fugacity may be computed directly using equation (36) or (37) once values for $a_{\text{SiO}_2(\text{aq})}$ are fixed by simultaneous forsterite–fluid equilibrium involving aqueous silica. In the present example, $a_{\text{SiO}_2(\text{aq})}$ values are buffered either by the less siliceous forsterite–chrysotile equilibrium (14) or by the more siliceous forsterite–talc equilibrium (16) (Fig. 1a). These $a_{\text{SiO}_2(\text{aq})}$ values were used to compute f_{O_2} via the SFM buffer. The results are shown in Fig. 1b for $P = 1$ kbar, $X_{\text{fa}} = 0.1$, and $a_{\text{H}_2\text{O}} = 1$. The f_{O_2} curve shows a slope change at $\sim 432^\circ\text{C}$, which corresponds to the phase change from chrysotile to talc. At temperatures below this slope change, $a_{\text{SiO}_2(\text{aq})}$ values fixed by the less siliceous forsterite–chrysotile assemblage result in more reduced f_{O_2} values. At temperatures above the slope change, $a_{\text{SiO}_2(\text{aq})}$ values fixed by the more siliceous forsterite–talc assemblage result in more oxidized f_{O_2} values. A more holistic view of the model assemblage is that olivine–serpentine–magnetite–fluid equilibrates at lower f_{O_2} than does olivine–talc–magnetite–fluid. This result is consistent with previous modeling of the retrograde serpentinization of peridotite versus pyroxenite at 500 bars, in which hydration of the more siliceous pyroxenite produced talc and was buffered to higher f_{O_2} values, and hydration of the less siliceous peridotite produced serpentine and was buffered to lower f_{O_2} (Klein *et al.*, 2013).

The dashed lines in Fig. 1b represent the standard rock buffers QFM and iron–magnetite (IM), which permit the petrological contextualization of the two assemblages buffered at SFM. The f_{O_2} values of the talc-equilibrated assemblage are above QFM, a redox potential more consistent with hydrothermal alteration of basalt (Shock, 1992; Lyons *et al.*, 2005), which is much less reducing than serpentinization. In contrast,

f_{O_2} buffered by the chrysotile-equilibrated assemblage drops precipitously toward highly reducing conditions as temperature decreases, even approaching the IM buffer. Near IM, the assumption of $a_{\text{H}_2\text{O}} = 1$ becomes less valid as the mole fraction of H_2 in the fluid increases, but this fact does not detract from the basic message of this diagram and of Frost & Beard (2007): that the low f_{O_2} values of serpentinites are linked to analogously low $a_{\text{SiO}_2(\text{aq})}$ values.

It bears emphasis that no claim is made here that a theoretical correlation between f_{O_2} and $a_{\text{SiO}_2(\text{aq})}$ is the only defining mathematical relationship governing serpentinite equilibria. In fact, algebraic inspection of equations (36) and (37) shows that changes in $a_{\text{SiO}_2(\text{aq})}$ at constant f_{O_2} could also be accommodated by shifting X_{fa} values, or that changes in X_{fa} at constant $a_{\text{SiO}_2(\text{aq})}$ may inversely affect f_{O_2} . Nevertheless, the present calculations are focused on the relative effects of pressure on $a_{\text{SiO}_2(\text{aq})}$ – f_{O_2} equilibria at constant X_{Fe} ; incorporation of variable iron content is reserved for future iterations.

MODEL PARAMETERS

The apparent standard state molar Gibbs free energies ($\Delta_a G^\circ$) for most minerals were computed using SUPRTBL (Zimmer *et al.*, 2016), a web-based version of SUPCRT92 (Johnson *et al.*, 1992) that uses the HP11 database (Holland & Powell, 2011). Owing to their absence in SUPCRTBL, free energies for additional Fe-bearing minerals were computed manually using the thermodynamic parameters listed in Table 3, adopted from the references listed therein. Cronstedtite is a mixed-valence serpentine, $(\text{Fe}_2^{2+}\text{Fe}^{3+})(\text{Fe}^{3+}\text{Si})\text{O}_5(\text{OH})_4$, with a ferri-Tschermak substitution yielding ferric iron on both the octahedral and tetrahedral sites. The iron in Fe³⁺-serpentine, $\text{Fe}_2^{3+}\text{Si}_2\text{O}_5(\text{OH})_4$, is completely ferric, with all Fe³⁺ present on the octahedral site. Values of $\Delta_a G^\circ$ for $\text{SiO}_2(\text{aq})$ and other aqueous species were extracted from the DEW model (Sverjensky *et al.*, 2014). For comparison, $\Delta_a G^\circ$ values for $a_{\text{SiO}_2(\text{aq})}$ were also computed from the water density model of Dolejš & Manning (2010), valid to 20 kbar, with water density values from SUPCRTBL and the HP11 database. Standard states were selected to be the pure phase at P and T for minerals and H_2O , the pure phase at T and 1 bar for

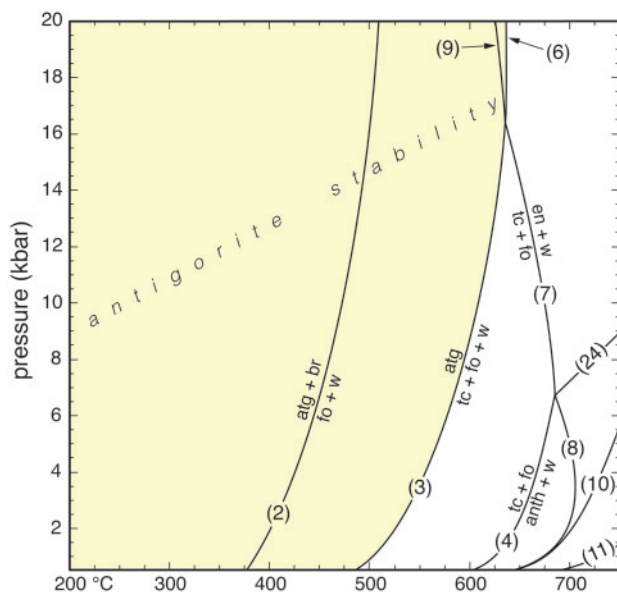


Fig. 2. Selected equilibria in the MgO–SiO₂–H₂O system for 0.5–20 kbar and 200–750 °C. The yellow shaded area represents the stability region of assemblages containing antigorite, the high-grade form of serpentine, with lizardite and chrysotile suppressed. Phase abbreviations are shown in Table 1. Curves are labeled with corresponding reaction numbers in Table 2. All equilibria are H₂O-saturated (*a*H₂O = 1) except reaction (24), which is H₂O-free.

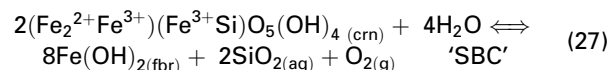
gases, and a one-molal solution referenced to infinite dilution at *P* and *T* for dissolved aqueous species.

Except for adopting chrysotile in the introductory example, antigorite was selected as the Mg-serpentine mineral of interest, given that it is the only stable serpentine form over the higher *P* and *T* range relevant to this study (Ulmer & Trommsdorff, 1995). To illustrate its stability range, a phase diagram in the system MgO–SiO₂–H₂O was constructed for 0.5–20 kbar and 200–800 °C (Fig. 2). There is disagreement in the literature as to the stability range of chrysotile and lizardite at lower grades, with reported upper limits ranging from as low as zeolite and prehnite–pumpellyite metamorphic grades (O’Hanley *et al.*, 1989) to ~300 °C at middle blueschist or greenschist facies (Evans, 2004) to as high as ~390 °C at upper blueschist- or greenschist-facies conditions (Schwartz *et al.*, 2013). However, these lower-grade serpentine minerals are suppressed from the calculations owing to the small differences in $\Delta_a G^\circ$ among antigorite, chrysotile, and lizardite (Frost & Beard, 2007; Evans, 2008). This approach is justified by test calculations over the temperature range 100–300 °C confirming that the positions of the antigorite–brucite and chrysotile–brucite equilibria differ by no more than 25–50 °C and 0.2–0.3 log units of *a*SiO_{2(aq)}, a minor difference compared with the overall range in model output.

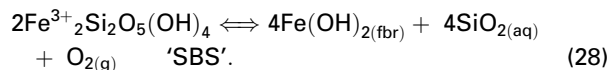
Redox buffers were selected to be broadly representative of those proposed in the serpentinite literature. The first redox buffer is SFM with *a*SiO_{2(aq)} buffered by the following sequence of forsterite–Mg-silicate equilibria that spans the entire temperature range of the

model, from high *T* to low *T*: forsterite–enstatite [equilibrium (23)], forsterite–anthophyllite [equilibrium (17)], forsterite–talc [equilibrium (16)], forsterite–antigorite [equilibrium (15)], and forsterite–antigorite–brucite [equilibrium (22)]. It should be noted that the assemblage forsterite–antigorite–brucite is invariant at *a*H₂O = 1 but may evolve to lower temperatures as *a*H₂O decreases. Fluid compositions were computed for the entire stability range of fo–atg–br at reduced water activity, although previous reaction path modeling of serpentinization at 500 bar suggests that this assemblage may only exist over a restricted ~50 °C wide temperature window at the upper stability limit of brucite (Klein *et al.*, 2009, 2013). Moreover, when serpentine–brucite assemblages are reported in retrograde serpentinites, they are not typically in textural equilibrium with olivine (e.g. Klein *et al.* 2009; Frost *et al.*, 2013; Schwarzenbach *et al.*, 2016). Therefore, as temperature decreases toward the lower limit of the model, this reaction should be treated with some degree of caution, more as a theoretical thermodynamic construct except where petrographically justified.

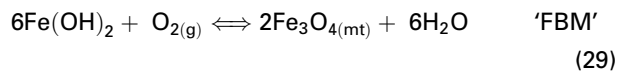
The remaining three buffers involve Fe-brucite in redox equilibrium with Fe-serpentine or magnetite. The Fe-brucite–Fe-serpentine buffers [equilibria (27 and 28)] are equilibrated at *a*SiO_{2(aq)} values buffered by the antigorite–brucite silica buffer [reaction (12)]. The selected Fe-serpentine components are cronstedtite and Fe³⁺-serpentine, both of which have been considered in previous studies that suggest ferric iron is preferentially hosted by serpentine—not magnetite—at lower temperatures (e.g. <200 °C; Seyfried *et al.*, 2007; Evans, 2008; Klein *et al.*, 2009, 2013). Published Mössbauer analyses suggest that both components are present simultaneously in natural serpentine minerals (Klein *et al.* 2009), but each is considered separately here in the assemblages silica–Fe-brucite–cronstedtite (SBC):



and silica–Fe-brucite–Fe³⁺-serpentine (SBS):



The Fe-brucite–magnetite buffer (FBM) is silica-independent and may be expressed as



following the formulation of Klein *et al.* (2013), who invoked the reaction to explain magnetite saturation in equilibrium with brucite.

Ideal mixing was assumed for all Mg–Fe minerals, with the acknowledgment that some minerals may exhibit nonideal mixing over the *P*–*T* range of the study, including olivine (Evans *et al.*, 2012) and brucite (McCollom & Bach, 2009). Values for *X*_{Fe} are fixed,

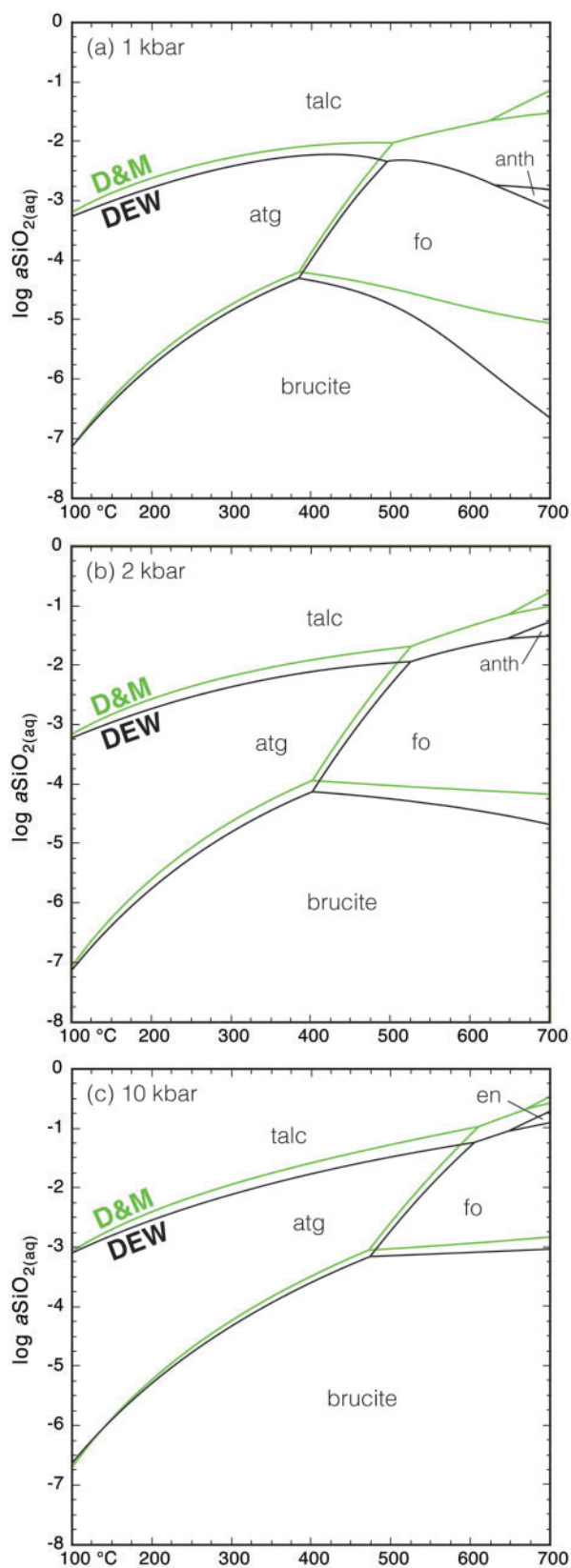


Fig. 3. Comparison of $a\text{SiO}_{2(\text{aq})}$ values computed in the system $\text{MgO-SiO}_2\text{-H}_2\text{O}$ using the DEW model (black) and the water density model of Dolejš & Manning (2010) (D&M; green). All minerals are pure endmembers; $a\text{H}_2\text{O} = 1$.

although previous reaction path modeling suggests that the redox state and mole fraction of Fe vary with temperature and bulk composition (Klein *et al.*, 2009; McCollom & Bach, 2009). Additionally, iron content of serpentine may increase by a per cent or two over the pressure range of the model, as implied by petrographic analysis of serpentinite clasts exhumed from the Marianas forearc (Debret *et al.*, 2014). In full acknowledgment of such complications, the model proceeds with fixed, average mineral compositions based on literature values as follows. For the SFM buffer, X_{Mg} values used for silica-buffering assemblages were selected to reflect average natural and calculated values in serpentinites (Klein *et al.*, 2009, 2013; McCollom & Bach, 2009): olivine, 0.90; brucite, 0.80; antigorite, 0.95; talc, 0.90; anthophyllite, 0.90; orthopyroxene, 0.90. For the SBS, SBC, and FBM buffers, X_{Mg} in brucite was constrained following the work of Klein *et al.* (2013), which suggested that magnetite-brucite controls redox at the upper temperature range of brucite stability, where X_{Mg} in brucite is ~ 0.9 , and that serpentine-brucite plays a greater role as temperature decreases, where X_{Mg} approaches ~ 0.7 . To allow for this variation between assemblages, a higher value of $X_{\text{Mg}} = 0.9$ was assigned to brucite in FBM, and a lower value of $X_{\text{Mg}} = 0.7$ was assigned to brucite in SBS and SBC. The mole fractions of cronstedtite and ferric serpentine were assigned a value of $X = 0.02$, based the average reported proportion of Fe^{3+} -bearing components in natural serpentines (Klein *et al.*, 2009, 2013).

RESULTS

Isobaric plots of silica activity versus T in the system $\text{MgO-SiO}_2\text{-H}_2\text{O}$

Because $a\text{SiO}_{2(\text{aq})}$ is stipulated to be a fundamental parameter governing the present model, it is helpful to understand the P - T effects on the silica-buffering properties of ultramafic mineral assemblages in the system $\text{MgO-SiO}_2\text{-H}_2\text{O}$. Figures 3–4 present activity-temperature diagrams of selected fluid-saturated silicification reactions and their corresponding invariant points. All mineral phases are assumed to be pure; test calculations for ideal Mg-Fe solutions using the X_{Mg} values listed above introduced a minor effect: no equilibrium in Fig. 4 shifted by more than 10–20 °C relative to the curves computed for pure Mg endmembers.

Figure 3 is constructed to compare results between the DEW model and the water density model of Dolejš & Manning (2010) for selected ultramafic reactions at $a\text{H}_2\text{O} = 1$. Both models are in agreement within less than one-half of a log unit at all pressures and temperatures except at 1 kbar, where equilibria above ~ 500 °C diverge by as much as 1.5 log units. At $P = 2$ kbar and higher, this divergence disappears. This may be explained by uncertainty in the DEW model owing to a slight mismatch in the curve fit to 1 kbar quartz

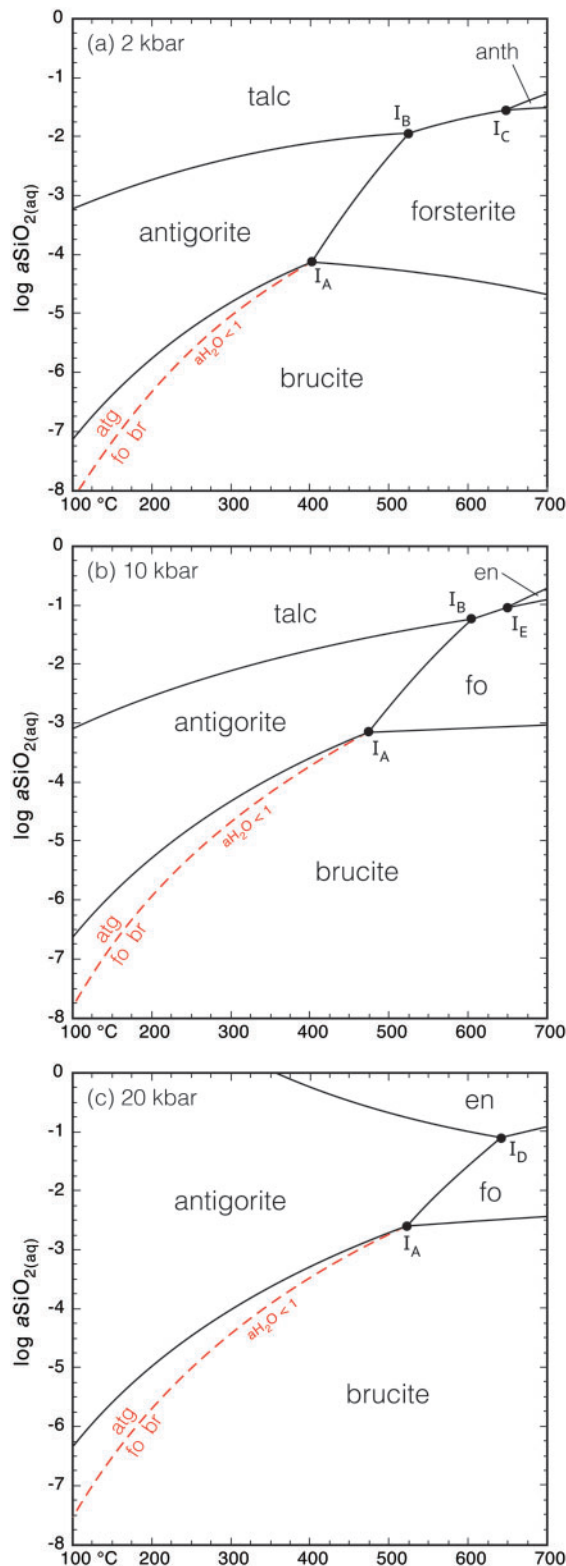
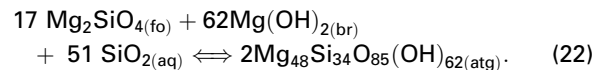


Fig. 4. The effect of P and T on silica-buffering, fluid-saturated equilibria in the system $\text{MgO}-\text{SiO}_2-\text{H}_2\text{O}$. All mineral phases are pure Mg-endmember compositions. Continuous lines and black dots correspond to, respectively, univariant equilibria and invariant points listed in Table 2. Water activity is unity except along the red dashed line, which corresponds to the down-temperature extension of the invariant assemblage forsterite-antigorite-brucite-fluid (I_A) as $a\text{H}_2\text{O}$ decreases (reaction (22)).

solubility data above 500 °C, compounded by extrapolation beyond the experimental data limit of 600 °C (see Fig. 7d of Sverjensky *et al.* 2014). Notwithstanding this uncertainty at 500–700 °C at 1 kbar, the DEW model was used for all subsequent fluid calculations owing to its internal consistency among all aqueous species considered in the model.

A set of isobaric DEW-based $a\text{SiO}_{2(\text{aq})}$ vs T plots at 2, 10, and 20 kbar is shown in Fig. 4. For all curves, water activity is unity, except along the red dashed curve, which tracks the theoretical position of the invariant point, I_A , with decreasing water activity (Frost & Beard, 2007). This curve represents the following equilibrium, constructed by adding reaction (2) to reaction (12):



This reaction permits the theoretical consideration of olivine stability over the low-temperature range of the model, with the caveat that many petrographic interpretations of retrograde serpentinites favor brucite-serpentine assemblages [e.g. reaction (12)] with no olivine over most or all of this same T range (see Model Parameters).

For most univariant equilibria, decreasing temperature results in lower $a\text{SiO}_{2(\text{aq})}$. All the antigorite-saturated curves have positive slopes at all pressures, indicating a direct monotonic relationship for serpentine between silica activity and temperature, except for antigorite-enstatite at 20 kbar, which has a negative slope. The curves in Fig. 4 with the lowest silica activities occur in equilibrium with brucite, predictive of low $f\text{O}_2$ in such assemblages, increasingly so as T decreases. Consistent with Fig. 1, talc always occurs at higher silica activities than antigorite. The highest silica activity occurs at the highest temperatures, where minerals with the highest Si-Mg ratios such as enstatite and anthophyllite are stable.

Isothermal increases in pressure generally cause increases in silica activity, the effect depending on the specific mineral assemblage. For example, $a\text{SiO}_{2(\text{aq})}$ fixed by the forsterite-antigorite-brucite invariant point, I_A , increases by about 1.5 log units from 2 kbar to 20 kbar, and the $a\text{SiO}_{2(\text{aq})}$ fixed by forsterite-brucite equilibrium at 600 °C increases by roughly two log units over the same pressure range. In contrast, $a\text{SiO}_{2(\text{aq})}$ fixed by forsterite-enstatite is roughly constant from 10 to 20 kbar.

Isobaric plots of $f\text{O}_2$ versus T

As described in the Model Parameters section, the silica-buffered Fe-bearing redox reactions under consideration are equilibrated with selected forsterite-bearing assemblages or with antigorite-brucite. Therefore, all other reactions in the $\text{MgO}-\text{SiO}_2-\text{H}_2\text{O}$ system shown in Figs 3 and 4 (e.g. antigorite-talc) were eliminated from subsequent redox calculations, resulting in the $f\text{O}_2$ - T diagrams shown in Figs 5 and 6. Unlike the preceding

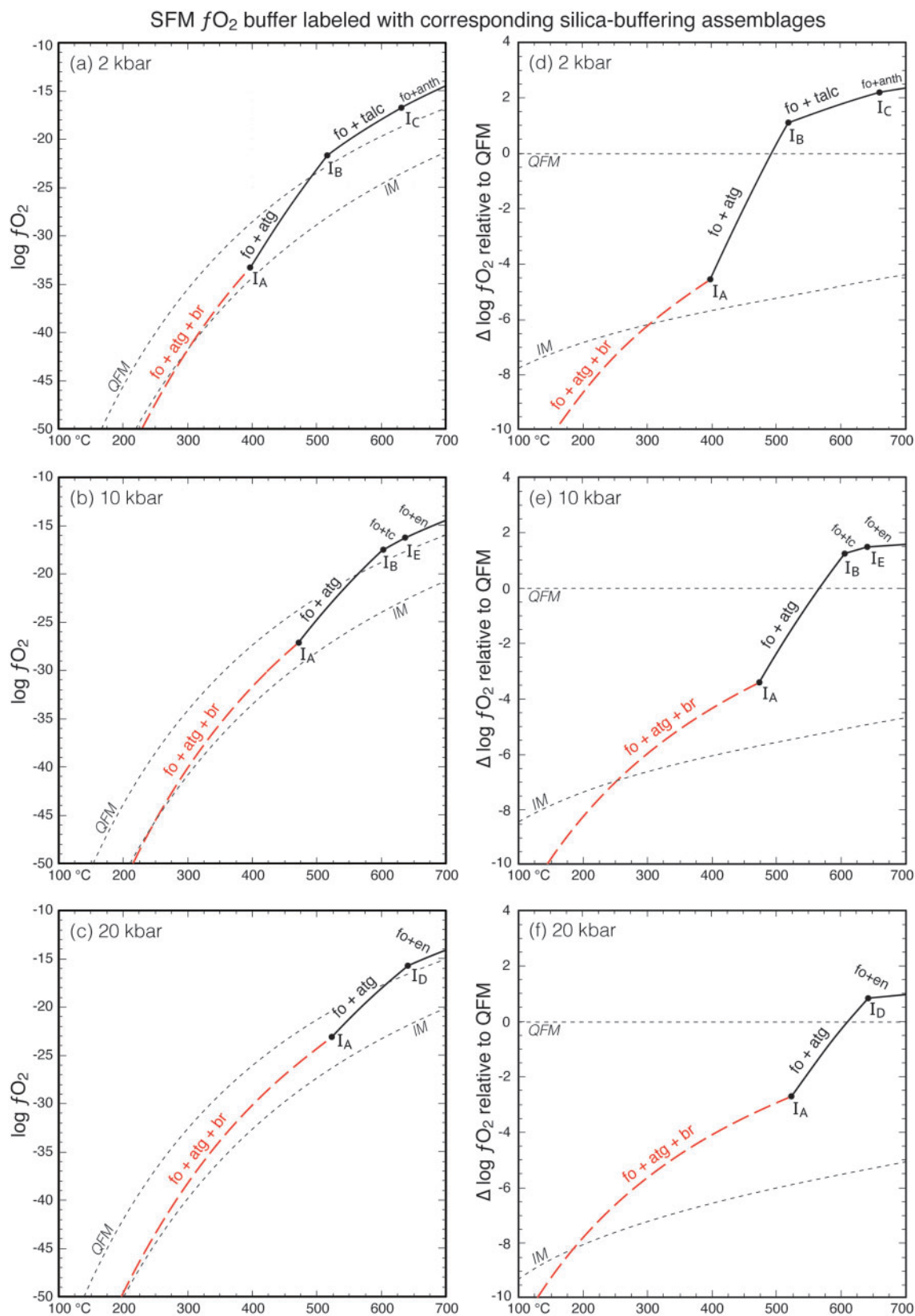


Fig. 5. The effect of P and T on fO_2 at SFM in the system $FeO-SiO_2-O_2$. (a–c) absolute fO_2 values. (d–f) fO_2 values relative to QFM. Line segments are labeled with the corresponding silica-buffering assemblages and invariant points in the system $MgO-SiO_2-H_2O$ (see Fig. 4). The red dashed line represents the down-temperature extension of the invariant assemblage forsterite–antigorite–brucite–fluid as aH_2O decreases [reaction (22)]. Dashed lines are the standard petrological buffers QFM and IM. X_{Mg} and X_{Fe} values are listed in the Model Parameters section.

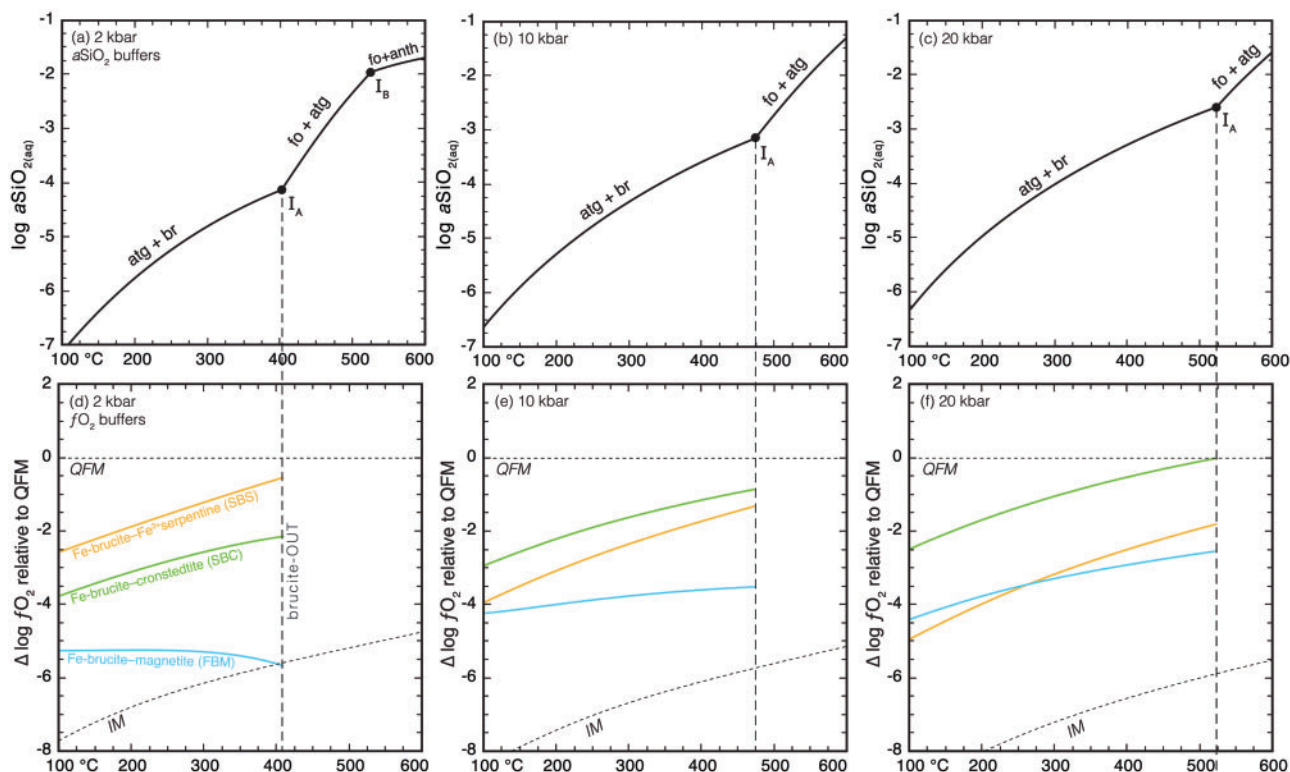


Fig. 6. The effect of P , T , and $a\text{SiO}_2$ on $f\text{O}_2$ for Fe-brucite buffers. (a–c) Selected silica buffers in the system $\text{MgO-SiO}_2\text{-H}_2\text{O}$ (continuous lines) with corresponding invariant points. (d–f) Fe-brucite redox buffers used in the model: fluid–fbr–crn [SBC, green, reaction (27), $X_{\text{fbr}} = 0.3$], fluid–fbr–fsrp [SBS, orange, reaction (28), $X_{\text{fbr}} = 0.3$], and fluid–fbr–mt [FBM, blue, reaction (29), $X_{\text{fbr}} = 0.1$]. SBC and SBS were calculated using $a\text{SiO}_2(\text{aq})$ from simultaneous equilibrium with antigorite–brucite in (a)–(c). Horizontal and curved dashed lines in (d)–(f) are the standard redox buffers QFM and IM respectively. The vertical dashed line is a graphic connection to align the plots along invariant point I_A and brucite-out. X_{Mg} and X_{Fe} values are listed in the Model Parameters section.

$a\text{SiO}_2(\text{aq})$ plots, water activity was permitted to vary in all redox calculations to constrain mass balance in the fluid at elevated hydrogen concentrations.

Figure 5 is a plot of $f\text{O}_2$ buffered by SFM versus T in equilibrium with all stable forsterite-bearing silica buffers at 2, 10, and 20 kbar (compare Fig. 4). Figure 5a–c shows absolute $f\text{O}_2$ values, and Fig. 5d–f shows $\Delta\log f\text{O}_2$ relative to QFM. The continuous black lines represent SFM with $a\text{SiO}_2(\text{aq})$ buffered by the univariant forsterite-bearing assemblages labeled in the figure. The dashed red line represents SFM with $a\text{SiO}_2(\text{aq})$ buffered by forsterite–antigorite–brucite and is given this contrasting graphic symbol to remind the reader that it represents the continuous position of the invariant point, I_A , with decreasing water activity.

To a first order, pressure does not affect the fundamental relationship that $f\text{O}_2$ of the SFM buffer increases with temperature and $a\text{SiO}_2(\text{aq})$ (see Fig. 4), because all slopes are positive at all pressures. However, pressure does affect the absolute $f\text{O}_2$ values of SFM, more so as temperature decreases. For example, at 400°C , $f\text{O}_2$ increases three log units from 2 to 20 kbar but is roughly constant at 600°C over the same pressure interval (Fig. 5a–c). Pressure also affects the relative difference between $f\text{O}_2$ of SFM and $f\text{O}_2$ of the standard petrological buffers QFM and IM (Fig. 5d–f). For example, the $f\text{O}_2$

of I_A is approximately QFM – 5 (five log units below QFM) at 2 kbar, QFM – 4 at 10 kbar, and QFM – 3 at 20 kbar.

Pressure exerts a more complex role on the relative positions of the Fe-brucite buffers SBS, SBC, and FBM (Fig. 6). For example, although the $\Delta f\text{O}_2$ of SBS and FBM at 300°C increases by ~ 2 log units from 2 to 20 kbar, the $\Delta\log f\text{O}_2$ of SBC decreases by ~ 1.5 log units over the same P range. Also, the slope of FBM is negative at 2 kbar and positive at higher pressures. At 200°C , SBS is the most oxidized Fe-brucite buffer at 2 kbar, but the most reduced at 20 kbar. Finally, IM is approached only by FBM at the lowest pressures. It should be noted that the calculated curves for the Fe-brucite buffers end discontinuously at the brucite-out temperature (vertical dashed lines).

P – T plots of fluid compositions

The variations in $a\text{SiO}_2$ and $f\text{O}_2$ described above imply that other redox-sensitive aqueous species are also sensitive to pressure, temperature, and choice of mineral assemblage. To explore such systematics over continuous P – T space, fluid compositions in equilibrium with the redox buffers SFM, SBS, SBC, and FBM were computed for 1–20 kbar and 100–700 $^\circ\text{C}$ with variable $a\text{H}_2\text{O}$

and fixed X_{Mg} values given in the Model Parameters section [Figs 7–15]. To place the calculations in context with the serpentinized forearc mantle and other geological and planetary settings with overlapping conditions, fluid compositions were superimposed onto graphic representations of selected petrological parameters, shown for reference in Fig. 7. In Fig. 7a, dashed lines represent univariant phase boundaries in the system $MgO-SiO_2-H_2O$, consistent with Fig. 2. The brucite-out boundary, representing the upper thermal stability of brucite, is highlighted by a thick white line. The large yellow shaded area represents the stability field of serpentine-bearing assemblages, assumed in the calculations to be 100% antigorite. Phase assemblages in black letters denote divariant silica-buffering assemblages, with the forsterite–antigorite–brucite assemblage at $a_{H_2O} < 1$ denoted in red. This black vs red color code is reproduced in the isopleths of subsequent P – T plots, with continuous black lines representing fluid compositions in equilibrium with a corresponding divariant assemblage in Fig. 7a, and red dashed lines representing fluid compositions at SFM with $a_{SiO_2(aq)}$ buffered by forsterite–antigorite–brucite.

In Fig. 7b, thick light-gray lines represent metamorphic facies boundaries (Winter, 2010). Blue arrows represent segments of tectonically representative subduction P – T pathways from a recent thermal model (van Keken et al., 2019). The pathways correspond to the slab surface, where fluids enter the mantle wedge to initiate ultramafic metamorphism. The steeper pathways for Honshu and Nicaragua represent subduction of older, colder lithosphere. The comparatively shallow pathway for Cascadia represents subduction of younger, warmer lithosphere. Blue dots represent equidistant points along the slab surface that are ~50 km from the trench, as measured graphically from the 0 °C starting point of each P – T pathway (see fig. 9 of van Keken et al., 2019).

Silica activity

Given the important role of silica activity in the present model, the P – T plot of $\log a_{SiO_2(aq)}$ is presented first (Fig. 8). In most regions of the plot, the $\log a_{SiO_2(aq)}$ isopleths have very steep slopes, indicating a much stronger dependence on temperature than on pressure, reflecting the results shown in Fig. 4. The pressure effect is quantifiable within the serpentine stability region as an increase of ~0.5–0.8 $\log a_{SiO_2(aq)}$ units when pressure increases isothermally from 1 to 20 kbar. In the region of brucite stability, pressure has a slightly greater effect on $a_{SiO_2(aq)}$ when buffered by antigorite–brucite (black) than when buffered by forsterite–antigorite–brucite (red). Within the talc, anthophyllite, and enstatite fields above ~3–4 kbar, the near-vertical isopleths are weakly dependent on pressure, if at all. Within the talc and anthophyllite stability regions below ~3–4 kbar, isopleths are near-horizontal, implying a strong dependence on P and weak dependence on T , but this result

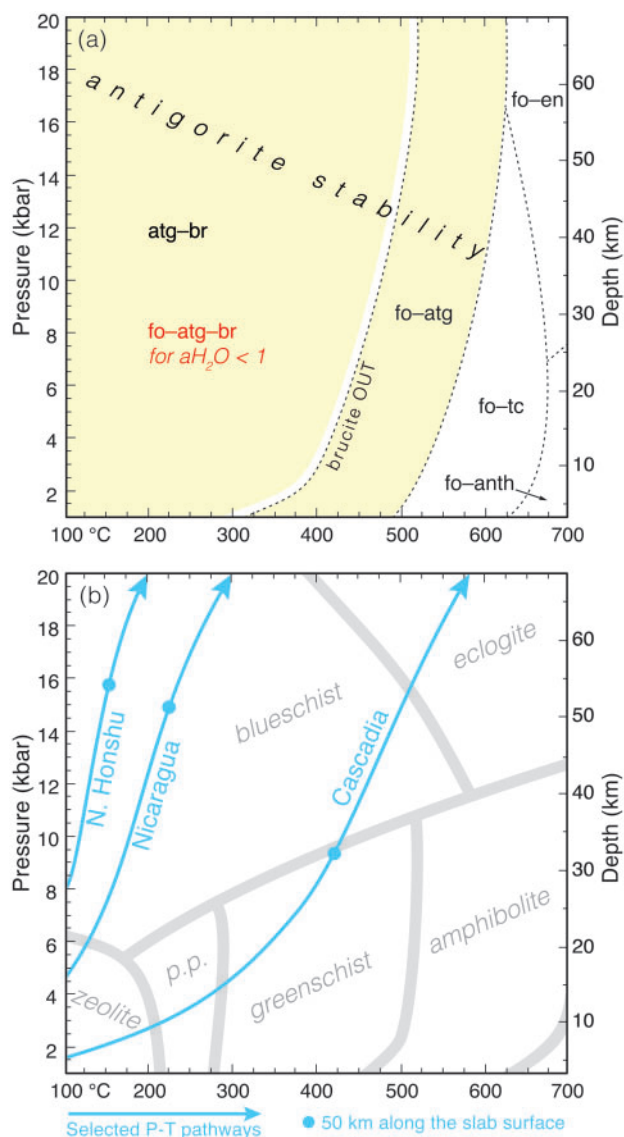


Fig. 7. Legend of symbols used in subsequent P – T plots. (a) The yellow region represents the stability of antigorite-bearing assemblages, with chrysotile and lizardite suppressed. Black letters denote the stability fields of mineral assemblages used to buffer silica activity, separated by thin dashed lines (see Fig. 4). The thick white line highlights the brucite-out curve. Red letters denote the stability field of forsterite–antigorite–brucite, applicable when $a_{H_2O} < 1$. (b) Blue arrows are pathways along the slab–mantle interface from van Keken et al. (2019). Cascadia is the model warm, shallow path; Honshu is the model cold, steep path. Blue dots represent equidistant locations along each path at 50 km from the trench. Thick gray lines are metamorphic facies boundaries; p.p., prehnite–pumpellyite facies.

coincides with the restricted P – T regime over which the uncertainty in the DEW $SiO_2(aq)$ data may be significant (see Model Parameters section and Fig. 3).

These properties may be placed in context with natural systems via comparative analysis of fluid compositions as a function of subduction pathway. Silica activity in Fig. 8 increases along all pathways as P and T increase; this increase is more pronounced along the warmer Cascadia path. For example, $a_{SiO_2(aq)}$ at 50 km

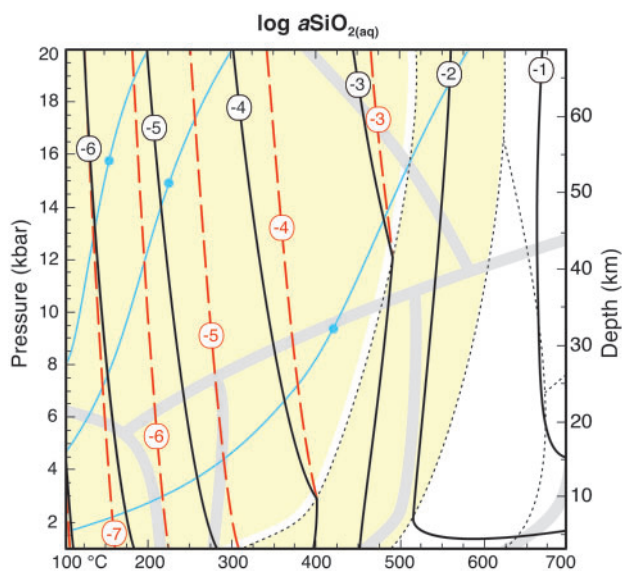


Fig. 8. Isopleths of $\log a\text{SiO}_{2(\text{aq})}$ vs P and T . Continuous black lines are in equilibrium with forsterite- or brucite-bearing assemblages, referenced in black in Fig. 7. Red dashed lines are silica-buffered by the assemblage forsterite–antigorite–brucite as $a\text{H}_2\text{O}$ decreases down-temperature.

slab distance is 2 log units greater along the warmer Cascadia path than on the cooler Honshu path. This strong dependence of $a\text{SiO}_{2(\text{aq})}$ on subduction pathway is another manifestation of the disproportionate influence of temperature relative to pressure.

Oxygen fugacity

Isopleths for absolute $f\text{O}_2$ are illustrated in Fig. 9 for the SFM, SBS, SBC, and FBM buffers. Similar to the result for $a\text{SiO}_{2(\text{aq})}$, the $f\text{O}_2$ values buffered by all redox assemblages are more strongly dependent on T than on P . Significant pressure effects on $f\text{O}_2$ do exist, however, with the largest variations occurring with the SBC and FBM buffers, where $\log f\text{O}_2$ increases by 5–6 units from 1 to 20 kbar. In contrast, the $\log f\text{O}_2$ isopleths of SBS are approximately vertical, suggesting little to no effect of pressure on oxygen fugacity for buffers in equilibrium with Fe^{3+} -serpentine, possibly owing to the absence of H_2O in the SBS reaction (28). At SFM, increasing pressure results in a slight decrease in $f\text{O}_2$ within the fo–atg field and an even smaller effect above the antigorite-out curve. In summary, pressure effects on $f\text{O}_2$ are present throughout the model P – T range, the effect depending on the assemblage. A notable outlier is SBS, which is the least pressure-sensitive of all redox buffers.

The differences in $f\text{O}_2$ buffered along each subduction pathway are qualitatively similar to corresponding trends for $a\text{SiO}_{2(\text{aq})}$ (Fig. 8). That is, increases in $f\text{O}_2$ are more significant along the shallow, warm path relative to the steep, cool path: Cascadia yields values ~ 25 – 30 log units greater than the Honshu path along identical slab distances, regardless of the buffering assemblage.

Relative pressure effects are more significant for $\Delta \log f\text{O}_2$ relative to QFM (Fig. 10) than for absolute $f\text{O}_2$. For example, the $\Delta \log f\text{O}_2$ isopleth slopes at SFM are negative when brucite is stable and positive when brucite is unstable. This leads to the result that isothermal increases in pressure cause $\Delta \log f\text{O}_2$ at SFM to increase in the presence of brucite and decrease in its absence. For the Fe-brucite buffers, SBS slopes are positive and the SBC and FBM slopes are mostly negative, indicating that increasing pressure will yield decreasing $\Delta \log f\text{O}_2$ for SBS and increasing $\Delta \log f\text{O}_2$ for SBC and FBM. These contrasting slopes also influence the evolution of $\Delta \log f\text{O}_2$ along the selected subduction P – T pathways, where positively sloped isopleths lead to greater variations in redox state between the warmer and cooler paths. For example, $\Delta \log f\text{O}_2$ values at 50 km slab distance at SBS are 2.5 log units greater on the warm Cascadia path than on the cool Honshu path, whereas the corresponding values at SBC and FBM differ by no more than one log unit. Also, because the SBS isopleths are subparallel to the P – T paths, $\Delta \log f\text{O}_2$ varies much less along subduction pathways at SBS than at SBC or FBM, where the isopleths intersect the P – T paths at much higher angles.

The values of $\Delta \log f\text{O}_2$ allow the calculations to be compared with previous estimates of the redox state of serpentinites. For the Fe-brucite buffers, $\Delta \log f\text{O}_2$ ranges roughly from -1 to -5 , broadly consistent with other calculations of low $f\text{O}_2$ values in serpentinites (e.g. Frost, 1985; Sleep *et al.*, 2004; Frost & Beard, 2007). For the SFM buffer, $\Delta \log f\text{O}_2$ values are ~ -4 to -6 at temperatures approaching brucite-out, consistent with previous work and comparable with the more reduced states of the SBS, SBC, and FBM buffers. A narrow window of the forsterite–antigorite field buffered by SFM lies above $\Delta \log \text{QFM} = 0$, and antigorite dehydrates at $\sim \Delta \log \text{QFM} = +1$. This is in broad agreement with the result of Piccoli *et al.* (2019), calculated for forearc conditions along the geotherm at ~ 25 – 27 kbar and ~ 550 – 625 °C. However, at the lowest temperatures, values for SFM in the forsterite–antigorite–brucite field approach 10–12 units below QFM, less than any previous calculation for serpentinites, reflecting the theoretical limits of the fo–atg–br assemblage.

Defining reduced fluids as having $f\text{O}_2$ values below QFM, Fig. 10 shows that all redox buffers that overlap the antigorite–brucite field can generate reduced fluids at all corresponding P and T , and along all subduction pathways. The SFM buffer with silica defined by forsterite–antigorite may generate reduced fluids except for the uppermost ~ 50 °C range of antigorite stability at all pressures. Only the Cascadia path intersects this zone of antigorite-stabilized, oxidized fluids, and only at eclogite grade. The SFM buffer defined by talc, enstatite, or anthophyllite equilibria never equilibrates with reduced fluids at any pressure. To summarize, reduced fluids can form only when antigorite is stable. Moreover, the special association of serpentine with reduced fluids exists for pressures up to 20 kbar and

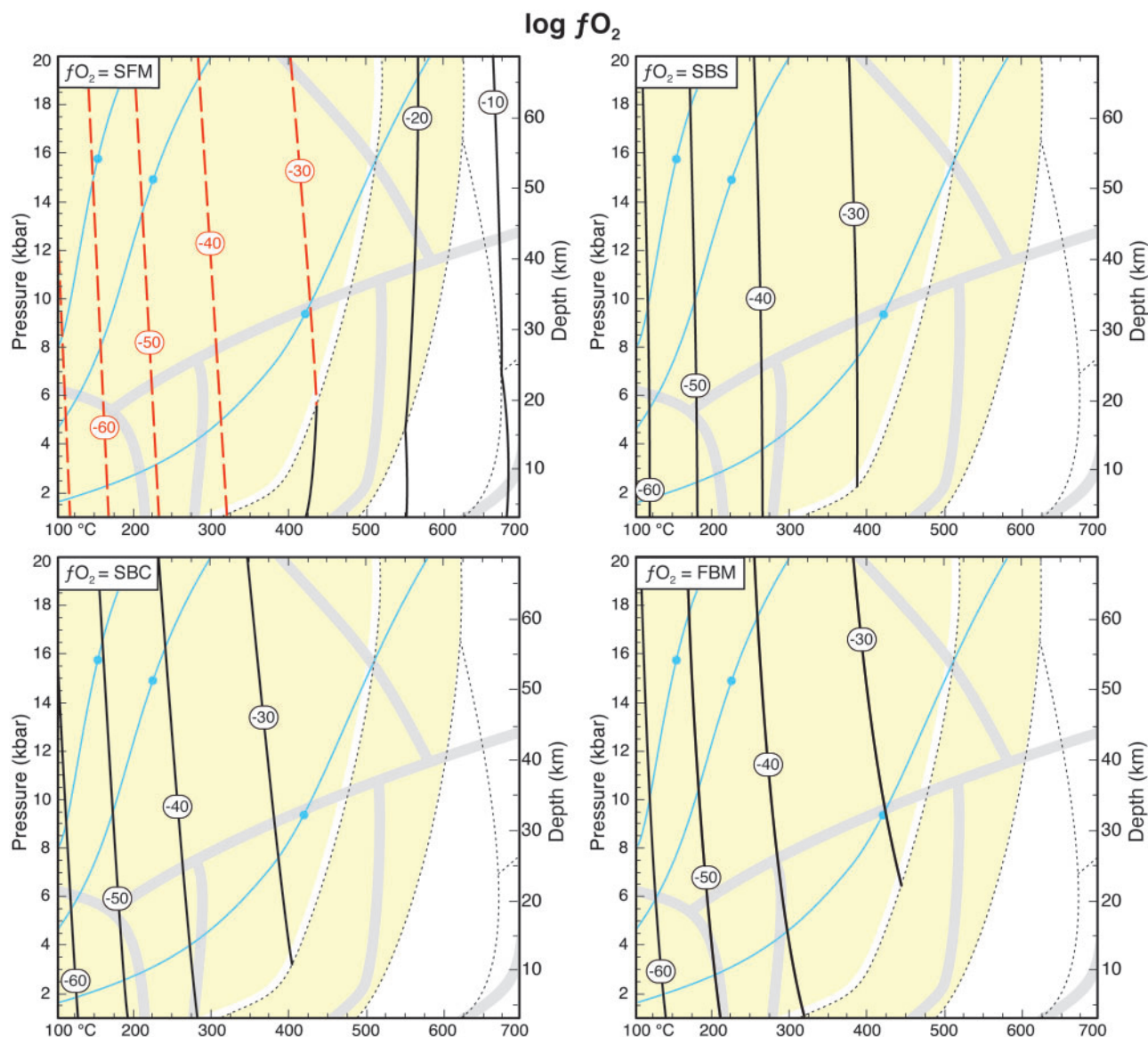


Fig. 9. Isopleths of $\log f_{O_2}$ vs P and T buffered by SFM, SBS, SBC, or FBM. (See Fig. 8 for description of black and red contours.)

probably beyond. Reduced fluids are predicted the entire length of all subduction paths, except the final segment of Cascadia. Although f_{O_2} may be considered to be low overall, the absolute f_{O_2} values within the reduced regime remain sensitive to pressure, temperature, and mineral assemblage.

Hydrogen

Variations of H_2 concentration owing to P and T were computed using reaction (30) and parameterized as $\log m_{H_2}$ (Fig. 11). For the SFM buffer, $\log m_{H_2}$ isopleths show irregular topologies, with slopes that vary significantly according to the silica-buffering assemblage. The irregularity of hydrogen concentration trends at SFM is highlighted in an isobaric plot that relates m_{H_2} to $a_{SiO_{2(aq)}}$ at 2 kbar and 100–700 $^{\circ}\text{C}$ (Fig. 12). Vertical dashed lines align the phase changes in the two plots to

facilitate the visual correlation of slope changes in $a_{SiO_{2(aq)}}$ and m_{H_2} . $\log a_{SiO_{2(aq)}}$ increases monotonically throughout the plot (Fig. 12b), whereas the accompanying $\log m_{H_2}$ trend changes from a negative to a positive slope when antigorite converts to talc (Fig. 12a). This slope change suggests that, as T increases, the relative thermodynamic drive for the reduction of H_2O to H_2 [reaction (30)] becomes stronger than the drive to increase in f_{O_2} via increasing $a_{SiO_{2(aq)}}$ (compare Figs 1 and 5).

Hydrogen concentrations buffered by SFM increase towards the origin where the fluid is saturated with H_2 -rich vapor. To illustrate this effect, hydrogen gas solubility data of Seward & Franck (1981), known up to 2.5 kbar, are plotted in Fig. 11 as black dots, to the left of which a vapor phase is stable. The dashed line and question mark represent a hand-drawn extrapolation beyond the P - T limit of the Seward & Franck data,

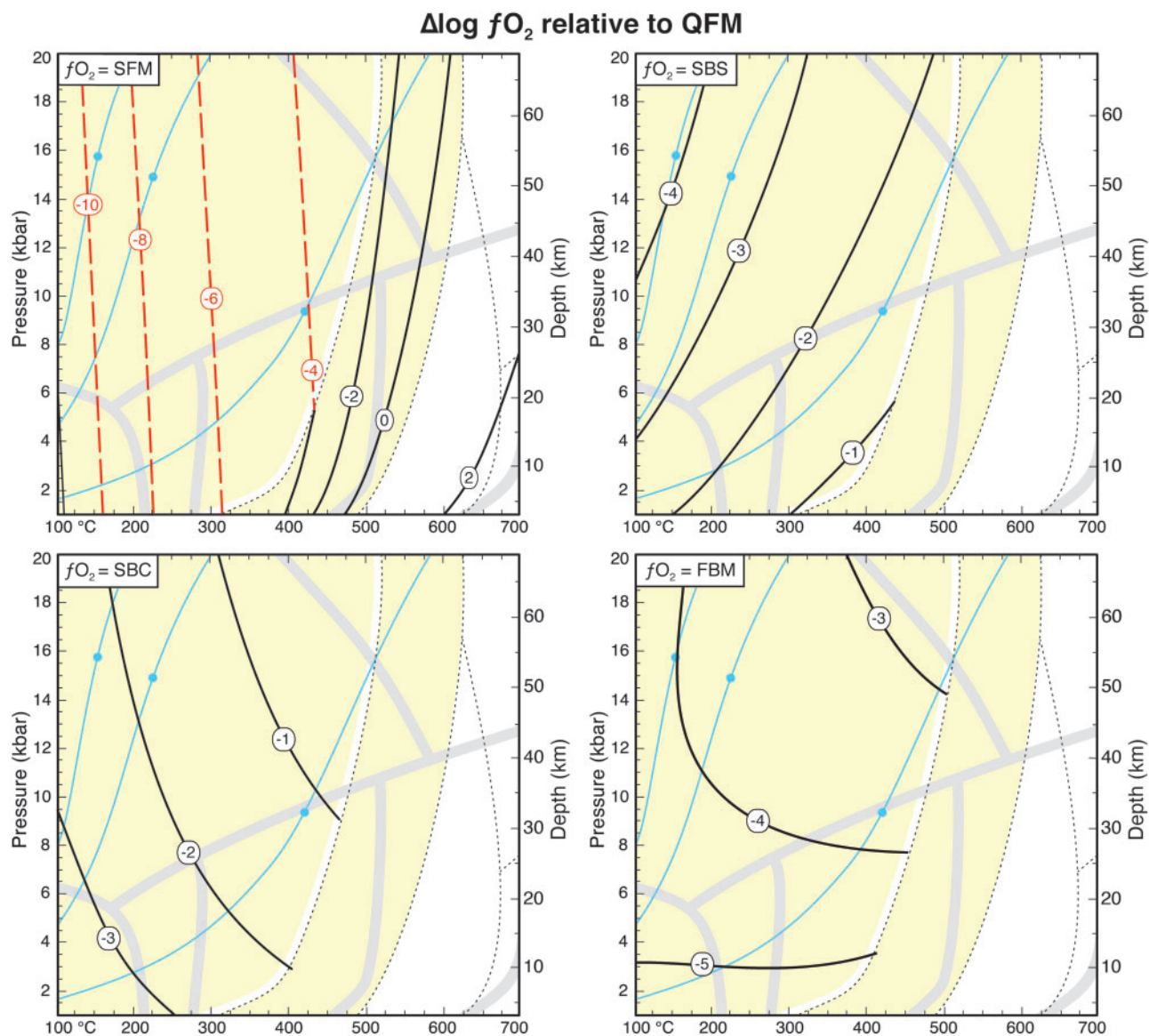


Fig. 10. Isopleths of $\Delta \log fO_2$ relative to QFM vs P and T , buffered by SFM, SBS, SBC, or FBM. (See Fig. 8 for description of black and red contours.)

which tentatively suggest that the vapor saturation curve approximately parallels the $\log mH_2 = 0.5$ isopleth. The vapor saturation curve is also plotted directly versus T at $P = 2$ kbar in Fig. 12. The results show that an H_2 -rich vapor is stable only at SFM, and only when silica is buffered by forsterite–antigorite–brucite at low aH_2O . No Fe-brucite buffer stabilizes a vapor phase, although FBM is very near vapor saturation at greenschist grade, with $\log mH_2$ between zero and 0.5.

Changes in mH_2 owing to pressure depend on the redox-buffering mineral assemblage. The Fe-brucite buffers (SBS, SBC, and FBM) yield isopleths with positive slopes, implying that isothermal pressure increases will lead to lower mH_2 . This pressure effect is more significant for SBC and FBM, which show a 4–5 log unit decrease in mH_2 from 1 to 20 kbar, compared with a two-log unit decrease for SBS. For SFM, pressure effects are

more significant for the forsterite–antigorite–brucite assemblage than for other more siliceous assemblages, whose approximately vertical isopleths show no more than one log unit change in mH_2 over the pressure range of the model.

The evolution of fluid compositions along a given P – T path also depends on the buffering assemblage. For Fe-brucite buffers, the positively sloped isopleths are approximately parallel to the P – T paths, which indicates that mH_2 does not vary by more than a log unit or two along individual subduction pathways. However, differences between paths are more significant: mH_2 values are 3–4 log units higher along the warmer Cascadia path than along the cooler Honshu path. For the SFM buffer, the opposite relationship is true: mH_2 varies by 4–5 log units along individual subduction paths, but no

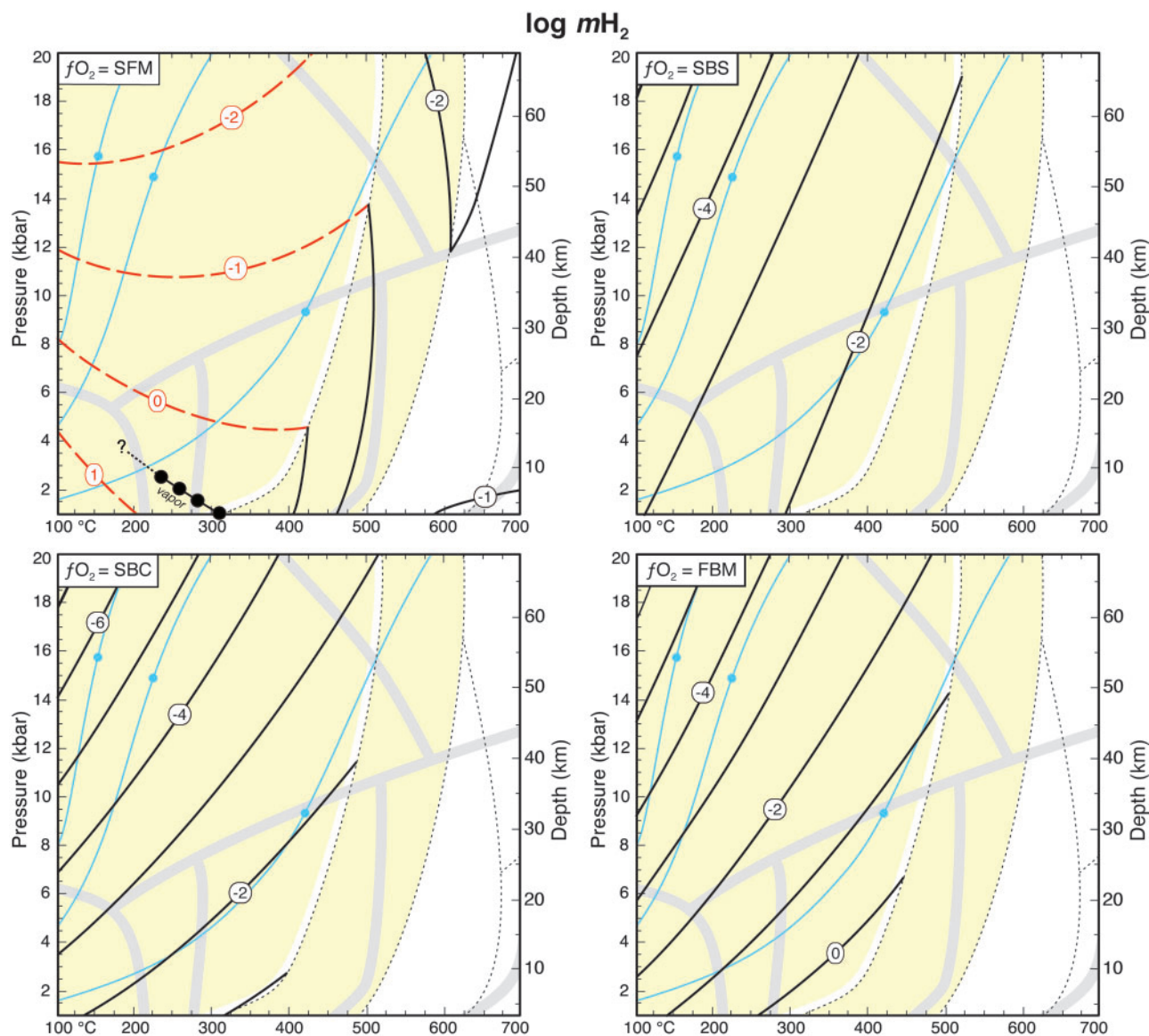


Fig. 11. Isopleths of $\log m\text{H}_2$ vs P and T , buffered by SFM, SBS, SBC, or FBM. (See Fig. 8 for description of black and red contours.)

more than 1–1.5 log units between equidistant points along all paths.

Carbon and sulfur

Concentrations of selected zerovalent, single-carbon or single-sulfur aqueous species were computed using reactions (31)–(33), and parameterized as ratios: $m\text{CH}_4/m\text{CO}_2$, $m\text{CO}/m\text{CO}_2$, and $m\text{H}_2\text{S}/m\text{SO}_2$. The use of such ratios allowed the thermodynamic analysis of relative C and S fluid speciations without independent constraints on bulk mole fractions; for example, by direct choice of X_C and X_S or by stipulating saturation with a mineral. The resulting C and S calculations are shown in Figs 13–15.

Higher-order alkanes (i.e. ethane and propane) were suppressed from the calculations because previous theoretical, field, and experimental studies suggested that

CH_4 is by far the most abundant carbon species in reduced C–O–H fluids (Kenney *et al.*, 2002; Kutcherov *et al.*, 2002; Mottl *et al.*, 2003; Sherwood Lollar *et al.*, 2006; McCollom & Seewald, 2007). Some of these studies suggested that ethane and longer-chain alkanes can form up to ~10% or so of the carbon fraction of a methane-rich fluid because the conditions that favor methane also favor the formation of a minor fraction of polymerized hydrocarbons. Given this parallel stability of CH_4 with other hydrocarbons, methane in the model may be considered a proxy for a mixture of all reduced carbon species.

Methane equilibration was assumed despite the suggestions of previous serpentinization studies that methanogenesis is kinetically impeded at seafloor P and T in favor of metastable, less-reduced species such as formaldehyde and methanol (McCollom & Seewald, 2003; Proskurowski *et al.*, 2006; Seewald *et al.*, 2006; Lang

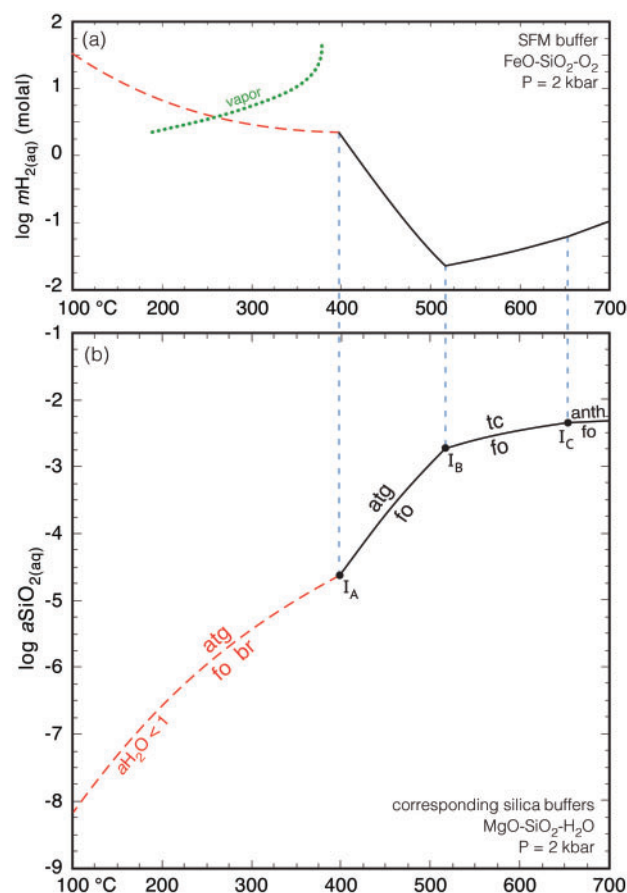


Fig. 12. Isobaric relationship of $m\text{H}_2$ and $a\text{SiO}_{2(\text{aq})}$. (a) Hydrogen concentrations at SFM with $a\text{SiO}_{2(\text{aq})}$ fixed by the silica buffers in (b). The green dotted line represents the vapor saturation curve from Seward & Franck (1981); an H_2 -rich vapor is stable to the left of this curve. (b) Silica buffers linked to SFM in (a) with invariant points aligned to $m\text{H}_2$ slope changes (vertical blue dashed lines). (See Fig. 8 for description of black and red curves.)

et al., 2010). This assumption is justified by the likelihood that equilibration in the forearc mantle is promoted by longer fluid residence times and, in some cases, temperatures greater than seafloor conditions. Moreover, previous experiments suggested that a few kilobars of pressure minimizes the kinetic barriers to methanogenesis that are otherwise observed in submarine serpentinite springs (Lazar et al., 2015).

$\log m\text{CH}_4/m\text{CO}_2$ isopleths (Fig. 13) show isothermal increases of 2–6 log units over the pressure range of the model, depending on the buffering assemblage. Higher ratios are favored by increasing pressure at SFM for brucite-free assemblages and at SBS. Lower ratios are favored by increasing pressure at SBC, FBM, and at SFM for forsterite–antigorite–brucite.

Similar to the P – T behavior of $\Delta\log f\text{O}_2$ in Fig. 10, where all reduced fluids are in equilibrium with antigorite, fluids that contain more CH_4 than CO_2 are also restricted to antigorite-bearing assemblages. When antigorite is destabilized, virtually all carbon in the fluid is speciated as CO_2 , indicating that the more siliceous

assemblages of forsterite–talca, forsterite–anthophyllite, and forsterite–enstatite produce fluids too oxidized to stabilize significant concentrations of methane. This result underscores the special link between serpentinites and methane-rich fluids (Horita & Berndt, 1999; McCollom & Seewald, 2001; McCollom et al., 2001; Klein et al., 2019).

Reflecting an analogous result for $\Delta\log f\text{O}_2$ (Fig. 10), the forsterite–antigorite field at SFM contains an $\sim 50^\circ\text{C}$ wide zone over which $\log m\text{CH}_4/m\text{CO}_2 < 0$; that is, where methane is less abundant than CO_2 . This low-methane zone suggests that serpentinites at their uppermost thermal stability limit do not promote productive methanogenesis. This geometry also implies that moderate P – T increases for a brucite-free serpentinite could transform the carbon speciation of a fluid from CH_4 -dominant to CO_2 -dominant. For example, at 475°C and 1 kbar, a fluid would be CO_2 -dominant with $\log m\text{CH}_4/m\text{CO}_2 \sim 1$, or 90% CO_2 ; but at 475°C and 3 kbar $\log m\text{CH}_4/m\text{CO}_2 \sim -1$, a fluid would be composed of 90% CH_4 .

$\log m\text{CH}_4/m\text{CO}_2$ values are strongly dependent on the P – T trajectory of each subduction pathway. At ~ 50 km along the slab surface, the Honshu fluid at SBC is characterized by $\log m\text{CH}_4/m\text{CO}_2 \sim 10$, and the Cascadia fluid shows $\log m\text{CH}_4/m\text{CO}_2 \sim 2$, a very large difference of 8 log units. Similar results obtain for SBS, FBM, and SFM. However, these pathway-dependent differences are mostly mathematical constructs of the calculations: whether $\log m\text{CH}_4/m\text{CO}_2$ equals 2 or 10 is not particularly meaningful geochemically because both compositions represent fluids in which $\sim 100\%$ of the carbon is methane. Therefore, a more practical conclusion from this analysis is that carbon in aqueous fluids along all subduction paths will be almost entirely speciated as CH_4 regardless of the P – T pathway of subduction. To further illustrate this point, the entire P – T range of the steep Honshu and Nicaragua pathways results in fluids with $\log m\text{CH}_4/m\text{CO}_2 > 4$, which is essentially pure methane. Similarly, the Cascadia slab–mantle interface stabilizes fluids with $\log m\text{CH}_4/m\text{CO}_2 > 0$ over its entire P – T pathway except for the final minor segment at eclogitic conditions, where $\log m\text{CH}_4/m\text{CO}_2$ becomes negative and CO_2 becomes proportionally more abundant.

The behavior of $m\text{H}_2\text{S}/m\text{SO}_2$ is analogous to that of $m\text{CH}_4/m\text{CO}_2$ in which isothermal increases in pressure are similarly dependent on the buffering assemblages and all fluids stabilized with antigorite strongly favor the reduced species, H_2S . At the equidistant 50 km points, the steeper Honshu path equilibrates fluids with $\log m\text{H}_2\text{S}/m\text{SO}_2$ values 10–12 units greater than the Cascadia path. Values for $\log m\text{H}_2\text{S}/m\text{SO}_2$ never decrease below ~ 5 – 6 along any P – T path, so that $m\text{H}_2\text{S} \gg m\text{SO}_2$ for all pathways. As with the case for methane, a practical conclusion from this analysis is that sulfur in serpentinite fluids will be almost entirely speciated as H_2S regardless of the P – T pathway of subduction.

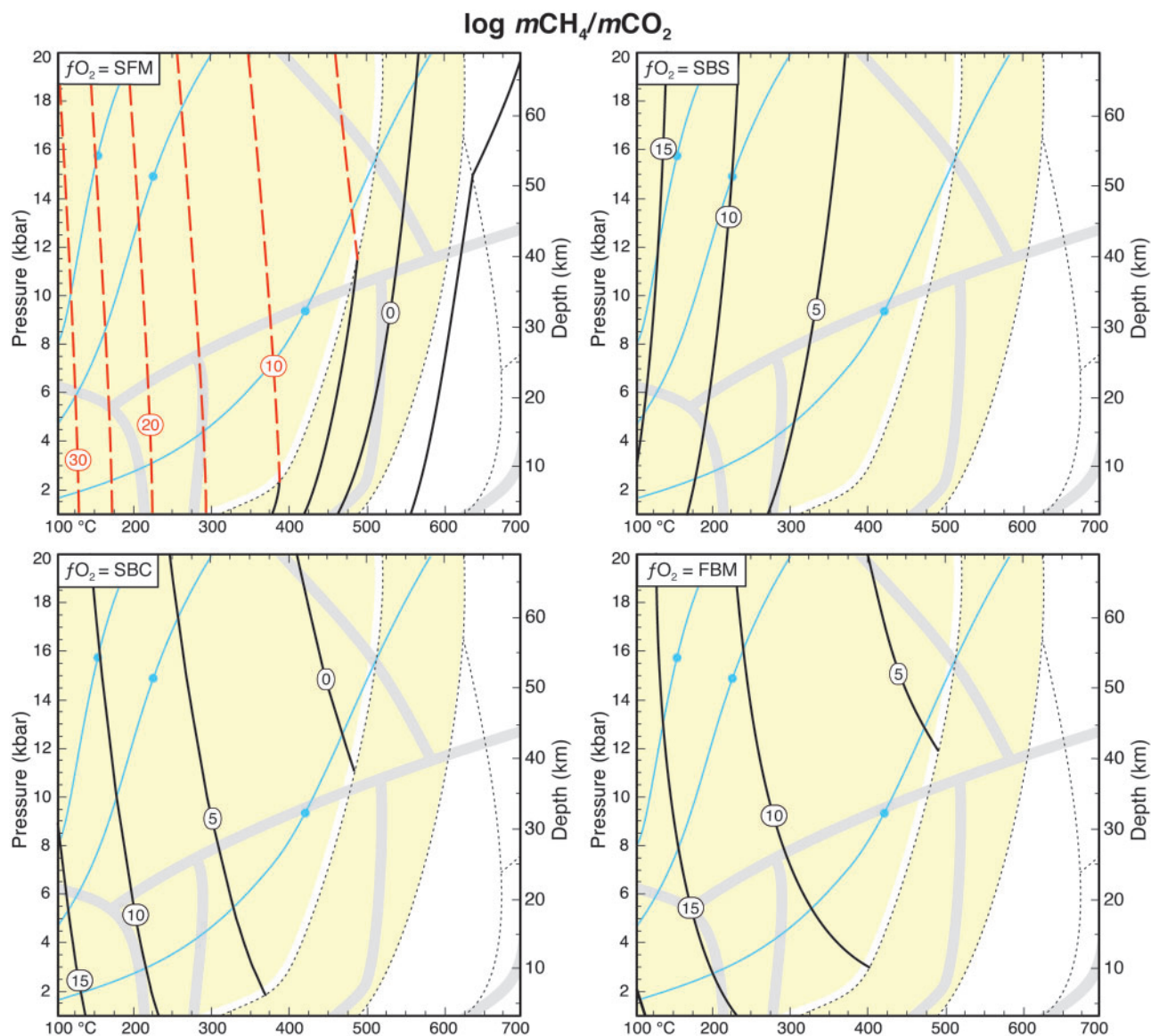


Fig. 13. Isopleths of $\log m\text{CH}_4/m\text{CO}_2$ vs P and T , buffered by SFM, SBS, SBC, or FBM. (See Fig. 8 for description of black and red contours.)

Isopleths for $\log m\text{CO}/m\text{CO}_2$ (Fig. 14) are topologically similar to those of $\log m\text{H}_2$ (Fig. 11), with irregular slopes for SFM and consistently positive slopes for all Fe-brucite buffers. For most P - T values, CO concentration is low compared with CO_2 , except towards the origin for SFM at forsterite-antigorite-brucite and at greenschist facies for FBM. For Fe-buffers, more CO is generated along the warmer Cascadia path, by several log units, than along the steeper paths. At SFM, all paths generate similar CO ratios, differing by no more than one-half of a log unit.

DISCUSSION

Comparison with reaction path models

As mentioned above, previous reaction path models of serpentinization at 500 bars (Klein *et al.*, 2009, 2013) have indicated that H_2 production depends partly on the

distribution of Fe among brucite, magnetite, and serpentine. A key schematic feature of these studies is a peak in H_2 concentration over the upper $\sim 100^\circ\text{C}$ range of brucite stability where $f\text{O}_2$ is buffered by Fe-brucite-magnetite equilibrium (FBM). Below this peak region, $m\text{H}_2$ decreases down-temperature as more Fe is stored in brucite as $\text{Fe}(\text{OH})_2$ and the governing mineral redox pair evolves to Fe-brucite-Fe-serpentine (SBS and/or SBC). Above the peak region, $m\text{H}_2$ decreases up-temperature because more Fe is stored in the fayalite component of olivine, where the governing mineral redox pair is fayalite-magnetite (SFM).

The present model cannot re-compute these reaction path models with precision, partly because the phase equilibria technique adopted here does not allow X_{Fe} to change continuously with temperature. However, the results may be used to broadly predict the pressure effects on the thermodynamic drive of the operative

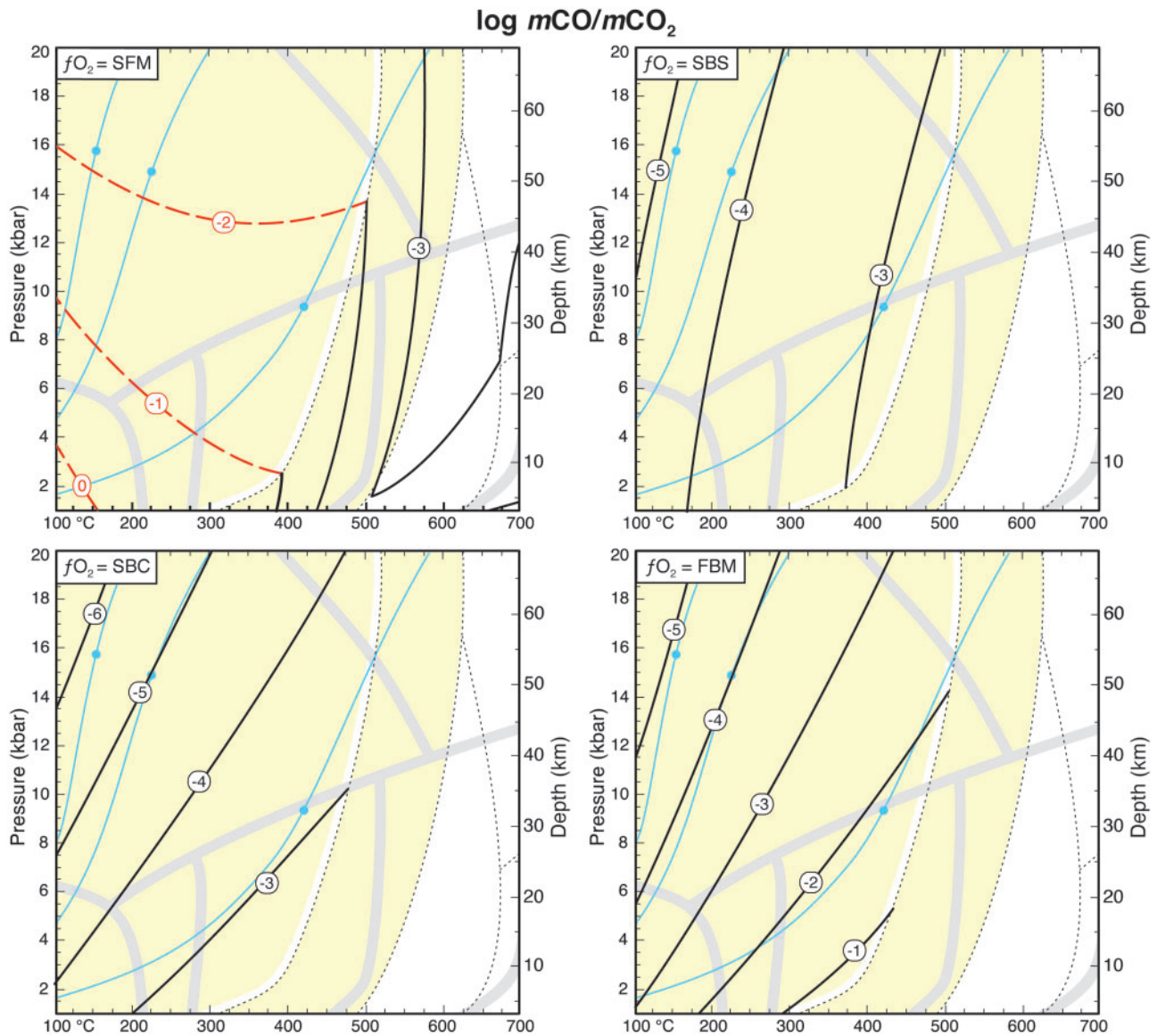


Fig. 14. Isopleths of $\log m\text{CO}/m\text{CO}_2$ vs P and T , buffered by SFM, SBS, SBC, or FBM. (See Fig. 8 for description of black and red contours.)

redox reactions in the Klein *et al.* studies. To make such predictions, $m\text{H}_2$ values fixed by the present redox buffers were plotted in Fig. 16 for $P=1$ and 5 kbar, from 100 to 400 °C. The thick gray line is hand-drawn on the plot to approximate the sum of $m\text{H}_2$ fixed by the selected buffers. This line reasonably re-creates the first-order trend of the Klein *et al.* studies, notably including the peak near brucite-out. The relationship of the approximate $m\text{H}_2$ to temperature and redox buffers is described as follows. As temperature decreases from 400 °C to brucite-in, the line parallels the SFM buffer where silica is fixed by forsterite–antigorite. At and below the brucite-in temperature, SFM is silica-buffered by forsterite–antigorite–brucite over an ~50 °C temperature range. This short segment is consistent with a restricted range of temperatures over which the Klein *et al.* studies reported the coexistence of olivine,

antigorite, brucite, and magnetite (see Model Parameters). The SFM segment is overlapped by FBM, which produces the highest $m\text{H}_2$ values. With a further decrease in T , $m\text{H}_2$ diverges from FBM values towards lower $m\text{H}_2$ values in equilibrium with the Fe-brucite–Fe-serpentine buffers, reflecting previous interpretations that the redox couple evolves down-temperature from FBM toward an Fe-bearing serpentine–brucite buffer such as SBC or SBS. As explained in the Model Parameters section, X_{fbr} was set to 0.1 for FBM and 0.3 for SBS and SBC. Although this imposed variation in X_{fbr} has a much lower resolution than the previous reaction path models, it allows for the relative positioning of the Fe-brucite buffers to be broadly consistent with Klein *et al.*; that is, lower $m\text{H}_2$ at lower temperatures buffered by serpentine (SBS and SBC) and higher $m\text{H}_2$ at higher temperatures buffered by magnetite (FBM).

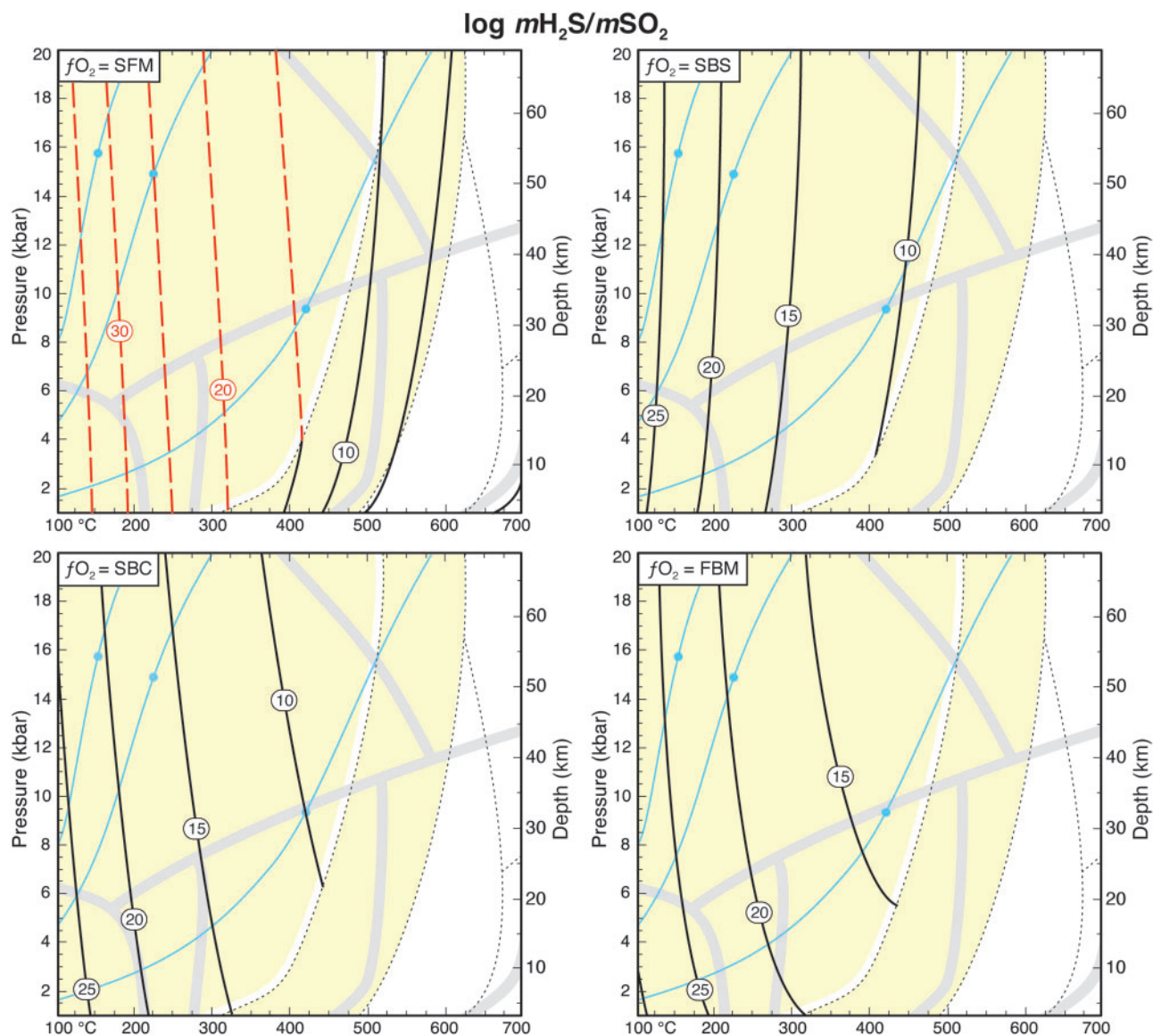


Fig. 15. Isoleths of $\log mH_2S/mSO_2$ vs P and T , buffered by SFM, SBS, SBC, or FBM. (See Fig. 8 for description of black and red contours.)

The framework established in Fig. 16 suggests three ways in which pressure may affect the reaction path models. First, the overall H_2 concentration is energetically favored to decrease with pressure, all else being equal, as shown by a change in peak $\log mH_2$ from ~ 1 at 1 kbar to roughly zero at 5 kbar. Second, all else being equal, the relative importance of cronstedtite versus Fe^{3+} -serpentine changes with pressure. Hydrogen concentrations at 1 kbar fixed by the cronstedtite-bearing buffer (SBC) are almost one log unit greater than hydrogen concentrations fixed by the buffer containing Fe^{3+} -serpentine (SBS). However, this difference decreases to ~ 0.1 – 0.2 log units at 5 kbar. Figure 11 shows that this shift continues to higher pressure: at 10 kbar, mH_2 at SBS is one log unit greater than at SBC. This implies that, if Fe-bearing serpentine is involved in buffering hydrogen concentrations, then cronstedtite is dominant

at $P \sim <5$ kbar and Fe^{3+} -serpentine is dominant at $P \sim >5$ kbar. Finally, the temperature of the H_2 peak shifts to higher temperatures with the pressure change from 1 to 5 kbar, although this is also predictable based on the underlying shift of brucite stability to higher temperatures as pressure increases, as shown in Fig. 2.

Effects on P – T paths

The present calculations may be used to predict general trends in how pressure affects serpentinite fluid compositions, with applications to subduction zones but also any terrestrial or planetary setting in which serpentinitization occurs at high pressure. The overall structure and diversity of the P – T trends in fluid compositions reflect the underlying properties of silica activity and oxygen fugacity to varying degrees.

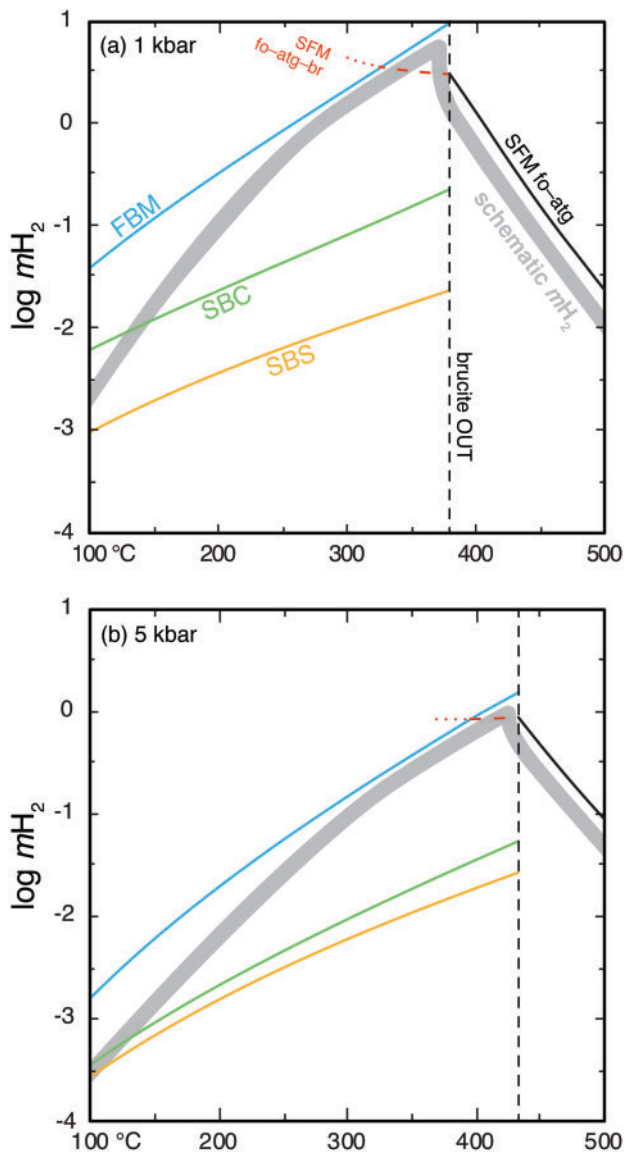


Fig. 16. Pressure effects on a schematic representation of hydrogen concentrations near the brucite-out temperature (vertical dashed line), qualitatively consistent with the reaction path models of Klein *et al.* (2009, 2013). The thick gray line is hand-sketched to approximate total hydrogen content as a function of redox buffer. This line diverges from FBM toward SBS and SBC to reflect the down-temperature partitioning of iron from magnetite to Fe-brucite and Fe³⁺-bearing serpentine components. X_{br} in brucite is 0.1 for FBM and 0.3 for SBS and SBC. X_{crn} and X_{fsrp} are 0.02. Black line: SFM with $a\text{SiO}_{2(\text{aq})}$ buffered by fo-atg. Red dashed line: SFM with $a\text{SiO}_{2(\text{aq})}$ buffered by fo-atg-br. FBM, SBC, and SBS are silica-buffered by atg-br.

The species with the most straightforward interpretations are methane and hydrogen sulfide. Many previous studies have agreed that CH₄ and H₂S are stable during serpentinization at seafloor pressures in high-temperature, magmatically driven hydrothermal systems (Charlou *et al.*, 2002; Konn *et al.*, 2009) and in off-axis, low-*T*, fault-enabled systems (Proskurowski *et al.*, 2008). Such submarine serpentinization occurs at pressures limited to hundreds of bars, but the present study points out that similarly reduced species may also be

stable in serpentinites over almost the entire *P-T* range relevant to subduction. Given the consistently high values of $m\text{CH}_4/m\text{CO}_2$ and $m\text{H}_2\text{S}/m\text{SO}_2$ throughout the model, subduction zones may be one of the most productive geological locations for the abiotic generation of reduced species such as methane and hydrogen sulfide.

Oxygen fugacity and silica activity are also similarly straightforward to interpret because the steeply sloped isopleths show a weak pressure effect. This trend implies that $f\text{O}_2$ and $a\text{SiO}_{2(\text{aq})}$ are systematically more enriched along shallow, warm subduction pathways relative to steep, cold pathways. In contrast, H₂ and CO show significant variations that strongly depend on pressure, temperature, and the choice of redox buffer. Nevertheless, the *P-T* plots of $m\text{H}_2$ and $m\text{CO}/m\text{CO}_2$ allow some first-order inferences; for example, for Fe-brucite buffers, shallow subduction paths are more likely to contain higher concentrations of CO than are cool, steep paths.

The results may be applied to the interpretation of redox variations in natural serpentinites. Evans *et al.* (2017) presented petrographic analyses of several subducted serpentinites, three of which contained magnetite, serpentine, and olivine, consistent with the SFM buffer. For each rock, *P* and *T* conditions were adapted from previous petrographic studies and combined with X_{H_2} values estimated from phase equilibria analyses of accessory mineral assemblages. Data for these three rocks, plus SFM for the same *P* and *T*, are compiled in Table 4. To a first order, the change in redox with *P* and *T* is consistent with the model, where $m\text{H}_2$ in the real and in model SFM rocks both decrease by roughly two log units from high to low grade. Despite certain chemical and mineralogical differences between the real rocks and the model assemblage (e.g. variations in X_{Fe} of the minerals) $m\text{H}_2$ values in two of the rocks (NC09-1a and GSZ-11a) are within one log unit of the model values. The third rock (NC07-60) contains $m\text{H}_2$ values that differ the most from SFM; however, this specimen also contains brucite, suggesting that Fe-brucite buffers may be more appropriate. In this case, the SBC buffer is -2.5 at 500 °C at 16 kbar, which would overlap the NC07-60 values within one $m\text{H}_2$ log unit. Evans *et al.* proposed that the redox state of the subducted serpentinites was imprinted primarily by pre-subduction processes; for example, degree of serpentinization in oceanic hydrothermal settings. However, the present model provides an alternative interpretation that the redox state of the natural rocks is consistent with equilibration of major mineral assemblages at subduction conditions to within one log unit. The remaining mismatch between the model and the rocks could be due to one or more of the following parameters: X_{Fe} in the minerals, saturation with additional minerals, variations in fluid and/or bulk-rock compositions, uncertainty in *P* and *T*, or energetic effects of real solutions.

Another recent study, by Piccoli *et al.* (2019), looked at the redox state along a prograde subduction

Table 4: mH_2 values in three serpentinites

Name*	P (kbar)	T (°C)	Log mH_2 (Evans <i>et al.</i>)*	Log mH_2 (SFM) [†]
NC09-1a	2	<300	-0.3	0.5
NC07-60	16	500–600	-3.3	-1.5 to -2
GSZ-11a	18–20	550–650	-3.3	-2 to -2.5

*Evans *et al.* (2017).

†Estimated from this study.

geotherm of serpentinites that contain olivine, magnetite, and antigorite, which may be modeled using SFM. The range of conditions in that study was ~ 500 – 800 °C and 24–30 kbar, which exceeds the conditions of the present model; however, two results of Piccoli *et al.* are consistent with the present model. First, at the low end of their range, they estimated $\Delta \log fO_2$ to be two units below QFM. Inspection of Fig. 10 shows that a minor extrapolation of SFM within fo-atg to 24 kbar at 500 °C yields a $\Delta \log fO_2$ value that is also approximately -2. Second, the relative topology of the Piccoli *et al.* calculations of $\Delta \log fO_2$ with increasing P and T is qualitatively similar to calculations presented in Fig. 5d–f, in which the positive slope of each successive segment of the SFM buffer generally decreases with increasing P and T . This trend diverges dramatically around 770 °C and 30 kbar, when the Piccoli *et al.* assemblage experiences chlorite dehydration and fO_2 plummets to several log units below QFM. This result would seem to contradict the present study, in which the highest temperature, highest silica assemblage leads to oxidized values at SFM. However, these very low fO_2 values were computed for an olivine–garnet–spinel–magnetite assemblage that contains only two silicate minerals, both Si-poor nesosilicates, implying much lower $aSiO_{2(aq)}$ than forsterite–enstatite and, by extension, much lower fO_2 . Therefore, the drop in redox state calculated by Piccoli *et al.* appears to be broadly consistent with the underlying $aSiO_{2(aq)}$ -based framework of the present study, albeit differing in specific choice of assemblage.

Not all calculations are consistent with the model, however. Debret & Sverjensky (2017) computed highly oxidized fO_2 values using the prograde assemblage antigorite–magnetite–olivine–clinocllore–tremolite. At 500 °C and 20 kbar, this assemblage yields fO_2 values near QFM, which is ~ 2 log units more oxidized than SFM at the same conditions (see Fig. 10) and more oxidized than the rocks in the studies by Evans *et al.* and Piccoli *et al.* at similar conditions. This oxidizing trend becomes even more divergent from SFM with increasing temperature: at 650 °C and 20 kbar, log fO_2 is 4–5 log units above QFM, which is 3–4 log units more oxidized than SFM. Based on the model parameters and details provided in the Debret & Sverjensky study, it is not clear why the calculations diverge so strongly from previous work and the current model, although the answer may be related to tremolite saturation or a more diverse array of fluid species. At a minimum, the proposition that a prograde serpentinite fluid can stabilize even hematite demonstrates that there is no consensus in the literature on the redox

potential of ultramafic metamorphism in subduction zones. Taken together, the models of Piccoli *et al.*, Evans *et al.*, Debret & Sverjensky, and the present contribution span a range of 7–8 log fO_2 units at eclogite conditions, indicating great variability in the redox state of high-pressure serpentinites depending on the mineral assemblage. A future improvement to the present model would include systematic testing of additional minerals and fluid components to explore the complexity of natural systems.

Astrobiological implications

Theories on the emergence of a biosphere from a lifeless planet often invoke prebiotic organic building blocks of methane and H_2S (Martin *et al.*, 2008; Lombard *et al.*, 2012; Patel *et al.*, 2015). Although the abiotic synthesis of prebiotic compounds has long been believed to occur in submarine serpentinite springs at oceanic P and T (Nisbet, 1985; Shock, 1990, 1992), the present model suggests that the reduced conditions favorable for the so-called primordial soup extend deep into the forearc mantle wedge. This suggestion is consistent with a recent paper citing field evidence for the subduction of active serpentinite seamount ecosystems along the Mariana forearc, in which the authors also proposed that subduction zones be included in hypotheses regarding the geological conditions favorable to the origin of life (Fryer *et al.*, 2020).

Seafloor serpentinitization has been proposed to generate food and energy sources for extremophile and chemolithoautotrophic microbes on Earth and other planets (Schulte *et al.*, 2006; McCollom & Seewald, 2007, 2013; Pons *et al.*, 2011). The present model extends this potential range to higher pressures than those of the terrestrial seafloor, consistent with recent thermal modeling that suggests life could be sustainable as deep as 10 km in the serpentinitized forearc mantle (Plümpner *et al.*, 2017). The general concept of biological activity at high pressure has been proposed by several previous researchers (Gold, 1992; Hazen *et al.*, 2002; Sharma *et al.*, 2002), and the present study contributes thermodynamic support for the viability of serpentinite-hosted habitats at depth in the forearc. However, the current modeling need not be restricted to terrestrial subduction settings. To the extent that serpentinitization may occur at similarly elevated pressures on the seafloors of planetary oceans (e.g. on Europa or Enceladus; Vance *et al.*, 2007, 2016; Glein *et al.*, 2015), the model predicts the availability of reduced fluids for deep extraterrestrial ecosystems on any planetary body with overlapping thermodynamic conditions.

Finally, reduced fluids in forearcs and deep planetary hydrothermal systems may have paleoclimatic implications. Methane has been proposed as an important terrestrial greenhouse gas during the early Precambrian, when the lithospheric flux of CO_2 was limited prior to the rise of oxygen (Pavlov *et al.*, 2000; Kasting, 2005; Emmanuel & Ague, 2007; Lazar *et al.*, 2012). The

serpentinized forearc mantle is a potential source of greenhouse methane. Such CH₄ is likely to be mobile on geological timescales because reduced carbon species in serpentinites are strongly partitioned into the fluid and are largely inert once formed. Upward percolation of methane through the serpentinized forearc mantle toward the atmosphere and hydrosphere may occur by diffuse degassing (Ingebritsen & Manning, 1999) or by focused flow along fractures and channels, with increasing efficiency as subduction temperatures decrease (Nakatani & Nakamura, 2016). Alternatively, serpentinization of the forearc mantle may permit organic compounds to be stored in fluid inclusions for later release, as has been recently proposed in a study of olivine-hosted fluid inclusions liberated by retrograde serpentinization in mid-ocean ridge systems (McDermott *et al.*, 2015; Klein *et al.*, 2019). Whether leaked directly or stored in fluid inclusions, the serpentinized forearc mantle wedge may have been an important source of greenhouse methane on the early Earth.

The above arguments outline the theoretical basis for a working hypothesis that a subducting planet has a higher probability than a non-subducting planet of developing and sustaining a biosphere. Subduction has probably occurred throughout most of Earth's history, a conjecture supported by a variety of independent lines of evidence. Phase equilibria analyses of mineral inclusions trapped inside Hadean zircons suggest that subduction zones have existed for at least 4.2 billion years (Hopkins *et al.*, 2010). Zinc isotope measurements also suggest that forearc settings similar to the modern Mariana system existed in the early Archean (Pons *et al.*, 2011). Based on the present model and references presented herein, it is tempting to wonder whether subduction influenced Earth's habitability and whether it may be useful as an additional predictive parameter in the search for life on other planets.

ACKNOWLEDGEMENTS

The author would like to thank Wolfgang Bach and an anonymous reviewer whose constructive criticisms greatly improved this paper. Thanks also go to Andreas Audétat for editorial handling, Craig Manning for discussions, and to Dimitri Sverjensky and colleagues for the development of the user-friendly DEW model. Suggestions from Emmanuel Codillo improved several of the figures. Special thanks go to Nancy Bryan for editorial refinement prior to submission.

FUNDING

Support for this work was provided by a PRISM grant from the CSUSB College of Natural Sciences.

REFERENCES

Barnes, I. & O'Neil, J. R. (1969). The relationship between fluids in some fresh alpine-type ultramafics and possible modern

- serpentinization, Western United States. *Geological Society of America Bulletin* **80**, 1947–1960. doi:10.1130/0016-7606(1969)80[1947:TRBFIS]2.0.CO;2.
- Barnes, I., O'Neil, J. R. & Trescases, J. J. (1978). Present day serpentinization in New Caledonia, Oman and Yugoslavia. *Geochimica et Cosmochimica Acta* **42**, 144–145. doi:10.1016/0016-7037(78)90225-9.
- Bostock, M. G., Hyndman, R. D., Rondenay, S. & Peacock, S. M. (2002). An inverted continental Moho and serpentinization of the forearc mantle. *Nature* **417**, 536–538. doi:10.1038/417536a.
- Brown, E. H., Wilson, D. L., Armstrong, R. L. & Harakal, J. E. (1982). Petrologic, structural, and age relations of serpentinite, amphibolite, and blueschist in the Shuksan Suite of the Iron Mountain–Gee Point area, North Cascades, Washington. *Geological Society of America Bulletin* **93**, 1087–1098. [https://doi.org/libproxy.lib.csusb.edu/10.1130/0016-7606\(1982\)93<1087:PSAARO>2.0.CO;2](https://doi.org/libproxy.lib.csusb.edu/10.1130/0016-7606(1982)93<1087:PSAARO>2.0.CO;2)
- Charlou, J. L., Donval, J. P., Fouquet, Y., Jean-Baptiste, P. & Holm, N. (2002). Geochemistry of high H₂ and CH₄ vent fluids issuing from ultramafic rocks at the Rainbow hydrothermal field (36°14'N, MAR). *Chemical Geology* **191**, 345–359. doi:10.1016/S0009-2541(02)00134-1.
- Coleman, R. G. (1986). *Field Trip Guide Book to New Idria Area, California. 14th General Meeting of the International Mineralogical Association*. International Mineralogical Association, Stanford University.
- Debret, B. & Sverjensky, D. A. (2017). Highly oxidising fluids generated during serpentinite breakdown in subduction zones. *Scientific Reports* **7**, 10351. <http://doi.org/10.1038/s41598-017-09626-y>
- Debret, B., Andreani, M., Muñoz, M., Bolfan-Casanova, N., Carlut, J., Nicollet, C., Schwartz, S. & Trcera, N. (2014). Evolution of Fe redox state in serpentine during subduction. *Earth and Planetary Science Letters* **400**, 206–218. <http://doi.org/10.1016/j.epsl.2014.05.038>
- Dick, H. J. B. (1974). Terrestrial nickel–iron from the Josephine Peridotite, its geologic occurrence, associations, and origin. *Earth and Planetary Science Letters* **24**, 291–298. doi:10.1016/0012-821X(74)90107-1.
- Dolejš, D. & Manning, C. E. (2010). Thermodynamic model for mineral solubility in aqueous fluids: theory, calibration and application to model fluid-flow systems. *Geofluids* **10**, 20–40. doi:10.1111/j.1468-8123.2010.00282.x.
- Emmanuel, S. & Ague, J. J. (2007). Implications of present-day abiogenic methane fluxes for the early Archean atmosphere. *Geophysical Research Letters* **34**, doi:10.1029/2007GL030532.
- Etiöpe, G., Schoell, M. & Hosgörmez, H. (2011). Abiotic methane flux from the Chimaera seep and Tekirova ophiolites (Turkey): Understanding gas exhalation from low temperature serpentinization and implications for Mars. *Earth and Planetary Science Letters* **310**, 96–104. doi:10.1016/j.epsl.2011.08.001.
- Evans, B. W. (2004). The serpentinite multisystem revisited: chrysotile is metastable. *International Geology Review* **46**, 479–506. doi:10.2747/0020-6814.46.6.479.
- Evans, B. W. (2008). Control of the products of serpentinization by the Fe₂₊-Mg₋₁ exchange potential of olivine and orthopyroxene. *Journal of Petrology* **49**, 1873–1887. doi:10.1093/petrology/egn050.
- Evans, B. W., Kuehner, S. M. & Chopelas, A. (2009). Magnetite-free, yellow lizardite serpentinization of olivine websterite, Canyon Mountain complex, N.E. Oregon. *American Mineralogist* **94**, 1731–1734. doi:10.2138/am.2009.3301.

- Evans, B. W., Dyar, M. D. & Kuehner, S. M. (2012). Implications of ferrous and ferric iron in antigorite. *American Mineralogist* **97**, 184–196. doi:10.2138/am.2012.3926.
- Evans, K. A., Reddy, S. M., Tomkins, A. G., Crossley, R. J. & Frost, B. R. (2017). Effects of geodynamic setting on the redox state of fluids released by subducted mantle lithosphere. *Lithos* **278–281**, 26–42. <http://doi.org/10.1016/j.lithos.2016.12.023>
- Frost, B. R. (1985). On the stability of sulfides, oxides, and native metals in serpentinite. *Journal of Petrology* **26**, 31–63. doi:10.1093/petrology/26.1.31.
- Frost, B. R. & Beard, J. S. (2007). On silica activity and serpentinization. *Journal of Petrology* **48**, 1351–1368. doi:10.1093/petrology/egm021.
- Frost, B. R., Evans, K. A., Swapp, S. M., Beard, J. S. & Mothersole, F. E. (2013). The process of serpentinization in dunite from New Caledonia. *Lithos* **178**, 24–39. <http://doi.org/10.1016/j.lithos.2013.02.002>
- Fryer, P., Wheat, C. G. & Mottl, M. J. (1999). Mariana blueschist mud volcanism: Implications for conditions within the subduction zone. *Geology* **27**, 103–106. [https://doi.org/libproxy.lib.csusb.edu/10.1130/0091-7613\(1999\)027<0103:MBMVIF>2.3.CO;2](https://doi.org/libproxy.lib.csusb.edu/10.1130/0091-7613(1999)027<0103:MBMVIF>2.3.CO;2)
- Fryer, P., Wheat, C. G., Williams, T., et al. (2020). Mariana serpentinite mud volcanism exhumes subducted seamount materials: implications for the origin of life. *Philosophical Transactions of the Royal Society of London, Series A* **378**, 20180425. doi:10.1098/rsta.2018.0425.
- Gerlach, D. C., AvéLallemant, H. G. & Leeman, W. P. (1981). An island arc origin for the Canyon Mountain ophiolite complex, Eastern Oregon, U.S.A. *Earth and Planetary Science Letters* **53**, 255–265. doi:10.1016/0012-821X(81)90158-8.
- Glein, C. R., Baross, J. A. & Waite, J. H. (2015). The pH of Enceladus' ocean. *Geochimica et Cosmochimica Acta* **162**, 202–219. doi:10.1016/j.gca.2015.04.017.
- Gold, T. (1992). The deep, hot biosphere. *Proceedings of the National Academy of Sciences of the USA* **89**, 6045–6049. doi:10.1073/pnas.89.13.6045.
- Hazen, R. M., Boctor, N., Brandes, J. A., Cody, G. D., Hemley, R. J., Sharma, A. & Yoder, H. S. (2002). High pressure and the origin of life. *Journal of Physics: Condensed Matter* **14**, 11489–11494. doi:10.1088/0953-8984/14/44/504.
- Holland, T. J. B. & Powell, R. (2011). An improved and extended internally consistent thermodynamic dataset for phases of petrological interest, involving a new equation of state for solids. *Journal of Metamorphic Geology* **29**, 333–383. doi:10.1111/j.1525-1314.2010.00923.x.
- Hopkins, M. D., Harrison, T. M. & Manning, C. E. (2010). Constraints on Hadean geodynamics from mineral inclusions in >4 Ga zircons. *Earth and Planetary Science Letters* **298**, 367–376. doi:10.1016/j.epsl.2010.08.010.
- Horita, J. & Berndt, M. E. (1999). Abiogenic methane formation and isotopic fractionation under hydrothermal conditions. *Science* **285**, 1055–1057. doi:10.1126/science.285.5430.1055.
- Hyndman, R. D. & Peacock, S. M. (2003). Serpentinization of the forearc mantle. *Earth and Planetary Science Letters* **212**, 417–432. doi:10.1016/S0012-821X(03)00263-2.
- Ingebritsen, S. E. & Manning, C. E. (1999). Geological implications of a permeability–depth curve for the continental crust. *Geology* **27**, 1107–1110. [10.1130/0091-7613\(1999\)027<1107:GIOAPD>2.3.CO;2](https://doi.org/10.1130/0091-7613(1999)027<1107:GIOAPD>2.3.CO;2)
- Johnson, J. W., Oelkers, E. H. & Helgeson, H. C. (1992). SUPCRT92: A software package for calculating the standard molal thermodynamic properties of minerals, gases, aqueous species, and reactions from 1 to 5000 bar and 0 to 1000°C. *Computers & Geosciences* **18**, 899–947. doi:10.1016/0098-3004(92)90029-Q.
- Kasting, J. (2005). Methane and climate during the Precambrian era. *Precambrian Research* **137**, 119–129. doi:10.1016/j.precamres.2005.03.002.
- Kenney, J. F., Kutcherov, V. A., Bendeliani, N. A. & Alekseev, V. A. (2002). The evolution of multicomponent systems at high pressures: VI. The thermodynamic stability of the hydrogen–carbon system: The genesis of hydrocarbons and the origin of petroleum. *Proceedings of the National Academy of Sciences of the USA* **99**, 10976–10981. doi:10.1073/pnas.172376899.
- Khedr, M. Z. & Arai, S. (2012). Petrology and geochemistry of prograde deserpentinized peridotites from Happo-O'ne, Japan: Evidence of element mobility during deserpentinization. *Journal of Asian Earth Sciences* **43**, 150–163. <http://doi.org/10.1016/j.jseas.2011.08.017>
- Klein, F. & Bach, W. (2009). Fe–Ni–Co–O–S phase relations in peridotite–seawater interactions. *Journal of Petrology* **50**, 37–59. doi:10.1093/petrology/egn071.
- Klein, F., Bach, W., Jöns, N., McCollom, T. M., Moskowitz, B. & Berquó, T. (2009). Iron partitioning and hydrogen generation during serpentinization of abyssal peridotites from 15°N on the Mid-Atlantic Ridge. *Geochimica et Cosmochimica Acta* **73**, 6868–6893. doi:10.1016/j.gca.2009.08.021.
- Klein, F., Bach, W. & McCollom, T. M. (2013). Compositional controls on hydrogen generation during serpentinization of ultramafic rocks. *Lithos* **178**, 55–69. doi:10.1016/j.lithos.2013.03.008.
- Klein, F., Grozeva, N. G. & Seewald, J. S. (2019). Abiotic methane synthesis and serpentinization in olivine-hosted fluid inclusions. *Proceedings of the National Academy of Sciences of the USA* **116**, 17666–17672. doi:10.1073/pnas.1907871116.
- Konn, C., Charlou, J. L., Donval, J. P., Holm, N. G., Dehairs, F. & Bouillon, S. (2009). Hydrocarbons and oxidized organic compounds in hydrothermal fluids from Rainbow and Lost City ultramafic-hosted vents. *Chemical Geology* **258**, 299–314. doi:10.1016/j.chemgeo.2008.10.034.
- Kutcherov, V. G., Bendeliani, N. A., Alekseev, V. A. & Kenney, J. F. (2002). Synthesis of hydrocarbons from minerals at pressures up to 5 GPa. *Doklady Physical Chemistry* **387**, 328–331. doi:10.1023/A:1021758915693.
- Lang, S. Q., Butterfield, D. A., Schulte, M., Kelley, D. S. & Lilley, M. D. (2010). Elevated concentrations of formate, acetate and dissolved organic carbon found at the Lost City hydrothermal field. *Geochimica et Cosmochimica Acta* **74**, 941–952. doi:10.1016/j.gca.2009.10.045.
- Lazar, C., McCollom, T. M. & Manning, C. E. (2012). Abiogenic methanogenesis during experimental komatiite serpentinization: Implications for the evolution of the early Precambrian atmosphere. *Chemical Geology* **326–327**, 102–112. doi:10.1016/j.chemgeo.2012.07.019.
- Lazar, C., Cody, G. D. & Davis, J. M. (2015). A kinetic pressure effect on the experimental abiogenic reduction of aqueous CO₂ to methane from 1 to 3.5 kbar at 300°C. *Geochimica et Cosmochimica Acta* **151**, 34–48. doi:10.1016/j.gca.2014.11.010.
- Leeman, W., Lallemant, H., Gerlach, D., Sutter, J. & Arculus, R. (1995). Petrology of the Canyon Mountain Complex, eastern Oregon. In: *Geology of the Blue Mountains Region of Oregon, Idaho, and Washington; Petrology and Tectonic Evolution of pre-Tertiary Rocks of the Blue Mountains Region. US Geological Survey, Professional Papers* **1438**, 1–43. 10.3133/pp1438.
- Lombard, J., López-García, P. & Moreira, D. (2012). The early evolution of lipid membranes and the three domains of life. *Nature Reviews Microbiology* **10**, 507–515. doi:10.1038/nrmicro2815.

- Lorand, J. P. (1988). Fe–Ni–Cu sulfides in tectonite peridotites from the Maqсад district, Sumail ophiolite, southern Oman: Implications for the origin of the sulfide component in the oceanic upper mantle. *Tectonophysics* **151**, 57–73. doi:10.1016/0040-1951(88)90240-5.
- Lyons, J. R., Manning, C. & Nimmo, F. (2005). Formation of methane on Mars by fluid–rock interaction in the crust. *Geophysical Research Letters* **32**.
- Martin, W., Baross, J., Kelley, D. & Russell, M. J. (2008). Hydrothermal vents and the origin of life. *Nature Reviews Microbiology* **6**, 805–814. doi:10.1038/nrmicro1991.
- McCollom, T. M. & Bach, W. (2009). Thermodynamic constraints on hydrogen generation during serpentinization of ultramafic rocks. *Geochimica et Cosmochimica Acta* **73**, 856–875. doi:10.1016/j.gca.2008.10.032.
- McCollom, T. M. & Seewald, J. S. (2001). A reassessment of the potential for reduction of dissolved CO₂ to hydrocarbons during serpentinization of olivine. *Geochimica et Cosmochimica Acta* **65**, 3769–3778. doi:10.1016/S0016-7037(01)00655-X.
- McCollom, T. M. & Seewald, J. S. (2003). Experimental constraints on the hydrothermal reactivity of organic acids and acid anions: I. Formic acid and formate. *Geochimica et Cosmochimica Acta* **67**, 3625–3644. doi:10.1016/S0016-7037(03)00136-4.
- McCollom, T. M. & Seewald, J. S. (2007). Abiotic synthesis of organic compounds in deep-sea hydrothermal environments. *Chemical Reviews* **107**, 382–401. doi:10.1021/cr0503660.
- McCollom, T. M. & Seewald, J. S. (2013). Serpentinites, hydrogen, and life. *Elements* **9**, 129–134. doi:10.2113/gselements.9.2.129.
- McCollom, T. M., Seewald, J. S. & Simoneit, B. R. T. (2001). Reactivity of monocyclic aromatic compounds under hydrothermal conditions. *Geochimica et Cosmochimica Acta* **65**, 455–468. doi:10.1016/S0016-7037(00)00533-0.
- McDermott, J. M., Seewald, J. S., German, C. R. & Sylva, S. P. (2015). Pathways for abiotic organic synthesis at submarine hydrothermal fields. *Proceedings of the National Academy of Sciences of the USA* **112**, 7668–7672. doi:10.1073/pnas.1506295112.
- Mottl, M. J., Komor, S. C., Fryer, P. & Moyer, C. L. (2003). Deep-slab fluids fuel extremophilic Archaea on a Mariana forearc serpentinite mud volcano: Ocean Drilling Program Leg 195. *Geochemistry, Geophysics, Geosystems* **4**. doi:10.1029/2003GC000588.
- Murray, M. & Lazar, C. (2019). Accessory minerals in New Idria serpentinites: implications for sulfur cycling in subduction zones. In: *CSUSB Meeting of the Minds*. California State University, San Bernardino.
- Nakatani, T. & Nakamura, M. (2016). Experimental constraints on the serpentinization rate of fore-arc peridotites: Implications for the upwelling condition of the slab-derived fluid. *Geochemistry, Geophysics, Geosystems* **17**, 3393–3419. doi:10.1002/2016GC006295.
- Nisbet, E. G. (1985). The geological setting of the earliest life forms. *Journal of Molecular Evolution* **21**, 289–298. doi:10.1007/BF02102361.
- O’Hanley, D. S., Chernosky, J. J. & Wicks, F. J. (1989). The stability of lizardite and chrysotile. *Canadian Mineralogist* **27**, 483–493.
- Palandri, J. L. & Reed, M. H. (2004). Geochemical models of metasomatism in ultramafic systems: serpentinization, rodingitization, and sea floor carbonate chimney precipitation. *Geochimica et Cosmochimica Acta* **68**, 1115–1133. doi:10.1016/j.gca.2003.08.006.
- Patel, B. H., Percivalle, C., Ritson, D. J., Duffy, C. D. & Sutherland, J. D. (2015). Common origins of RNA, protein and lipid precursors in a cyanosulfidic protometabolism. *Nature Chemistry* **7**, 301–307. doi:10.1038/nchem.2202.
- Pavlov, A. A., Kasting, J. F., Brown, L. L., Rages, K. A. & Freedman, R. (2000). Greenhouse warming by CH₄ in the atmosphere of early Earth. *Journal of Geophysical Research: Planets* **105**, 11981–11990. doi:10.1029/1999JE001134.
- Peretti, A., Dubessy, J., Mullis, J., Frost, B. R. & Trommsdorff, V. (1992). Highly reducing conditions during Alpine metamorphism of the Malenco peridotite (Sondrio, northern Italy) indicated by mineral paragenesis and H₂ in fluid inclusions. *Contributions to Mineralogy and Petrology* **112**, 329–340. doi:10.1007/BF00310464.
- Piccoli, F., Hermann, J., Pettke, T., Connolly, J. A. D., Kempf, E. D. & Vieira Duarte, J. F. (2019). Subducting serpentinites release reduced, not oxidized, aqueous fluids. *Scientific Reports* **9**, 19573. <http://doi.org/10.1038/s41598-019-55944-8>
- Plümpner, O., King, H. E., Geisler, T., Liu, Y., Pabst, S., Savov, I. P., Rost, D. & Zack, T. (2017). Subduction zone forearc serpentinites as incubators for deep microbial life. *Proceedings of the National Academy of Sciences of the USA* **114**, 4324–4329. doi:10.1073/pnas.1612147114.
- Pons, M.-L., Quitte, G., Fujii, T., Rosing, M. T., Reynard, B., Moynier, F., Douchet, C. & Albarede, F. (2011). Early Archean serpentine mud volcanoes at Isua, Greenland, as a niche for early life. *Proceedings of the National Academy of Sciences of the USA* **108**, 17639–17643. doi:10.1073/pnas.1108061108.
- Proskurowski, G., Lilley, M. D., Kelley, D. S. & Olson, E. J. (2006). Low temperature volatile production at the Lost City Hydrothermal Field, evidence from a hydrogen stable isotope geothermometer. *Chemical Geology* **229**, 331–343. doi:10.1016/j.chemgeo.2005.11.005.
- Proskurowski, G., Lilley, M. D., Seewald, J. S., Fruh-Green, G. L., Olson, E. J., Lupton, J. E., Sylva, S. P. & Kelley, D. S. (2008). Abiogenic hydrocarbon production at Lost City Hydrothermal Field. *Science* **319**, 604–607. doi:10.1126/science.1151194.
- Schulte, M., Blake, D., Hoehler, T. & McCollom, T. (2006). Serpentinization and its implications for life on the early Earth and Mars. *Astrobiology* **6**, 364–376. doi:10.1089/ast.2006.6.364.
- Schwartz, S., Guillot, S., Reynard, B., Lafay, R., Debret, B., Nicollet, C., Lanari, P. & Auzende, A. L. (2013). Pressure–temperature estimates of the lizardite/antigorite transition in high pressure serpentinites. *Lithos* **178**, 197–210. doi:10.1016/j.lithos.2012.11.023.
- Schwarzenbach, E. M., Caddick, M. J., Beard, J. S. & Bodnar, R. J. (2016). Serpentinization, element transfer, and the progressive development of zoning in veins: evidence from a partially serpentinized harzburgite. *Contributions to Mineralogy and Petrology* **171**, 1–22. <http://doi.org/10.1007/s00410-015-1219-3>
- Seewald, J. S., Zolotov, M. Y. & McCollom, T. (2006). Experimental investigation of single carbon compounds under hydrothermal conditions. *Geochimica et Cosmochimica Acta* **70**, 446–460. doi:10.1016/j.gca.2005.09.002.
- Seward, T. M. & Franck, E. U. (1981). The system hydrogen–water up to 440 °C and 2500 bar pressure. *Berichte der Bunsengesellschaft für Physikalische Chemie* **85**, 2–7. doi:10.1002/bbpc.19810850103.
- Seyfried, W. E., Jr, Foustoukos, D. I. & Fu, Q. (2007). Redox evolution and mass transfer during serpentinization: An

- experimental and theoretical study at 200 °C, 500 bar with implications for ultramafic-hosted hydrothermal systems at mid-ocean ridges. *Geochimica et Cosmochimica Acta* **71**, 3872–3886. <http://doi.org/10.1016/j.gca.2007.05.015>
- Sharma, A., Scott, J. H., Cody, G. D., Fogel, M. L., Hazen, R. M. & Hemley, R. J. (2002). Microbial activity at gigapascal pressures. *Science* **295**, 1514–1516. doi:10.1126/science.1068018.
- Sherwood Lollar, B., Lacrampe-Couloume, G., Slater, G. F., Ward, J., Moser, D. P., Gihring, T. M., Lin, L.-H. & Onstott, T. C. (2006). Unravelling abiogenic and biogenic sources of methane in the Earth's deep subsurface. *Chemical Geology* **226**, 328–339. doi:10.1016/j.chemgeo.2005.09.027.
- Shock, E. L. (1990). Geochemical constraints on the origin of organic compounds in hydrothermal systems. *Origins of Life and Evolution of the Biosphere* **20**, 331–367. doi:10.1007/BF01808115.
- Shock, E. L. (1992). Chemical environments of submarine hydrothermal systems. *Origins of Life and Evolution of the Biosphere* **22**, 67–107. doi:10.1007/BF01808019.
- Sleep, N. H., Meibom, A., Fridriksson, T., Coleman, R. G. & Bird, D. K. (2004). H₂-rich fluids from serpentinization: Geochemical and biotic implications. *Proceedings of the National Academy of Sciences of the USA* **101**, 12818–12823. doi:10.1073/pnas.0405289101.
- Sleep, N. H., Bird, D. K. & Pope, E. C. (2011). Serpentinite and the dawn of life. *Philosophical Transactions of the Royal Society of London, Series B* **366**, 2857–2869. doi:10.1098/rstb.2011.0129.
- Sverjensky, D. A., Harrison, B. & Azzolini, D. (2014). Water in the deep Earth: The dielectric constant and the solubilities of quartz and corundum to 60 kb and 1200 °C. *Geochimica et Cosmochimica Acta* **129**, 125–145. <http://doi.org/10.1016/j.gca.2013.12.019>
- Tsujimori, T., Liou, J. G. & Coleman, R. G. (2007). Finding of high-grade tectonic blocks from the New Idria serpentinite body, Diablo Range, California: Petrologic constraints on the tectonic evolution of an active serpentinite diapir. In: *Convergent Margin Terranes and Associated Regions: A Tribute to W. G. Ernst. Geological Society of America, Special Papers* **419**, 67–80. [https://doi.org/10.1130/2007.2419\(03\)](https://doi.org/10.1130/2007.2419(03)).
- Tutolo, B. M., Seyfried, W. E. & Tosca, N. J. (2020). A seawater throttle on H₂ production in Precambrian serpentinizing systems. *Proceedings of the National Academy of Sciences* **117**, 14756–14763.
- Ulmer, P. & Trommsdorff, V. (1995). Serpentine stability to mantle depths and subduction-related magmatism. *Science* **268**, 858–861. doi:10.1126/science.268.5212.858.
- Vance, S. D., Harnmeijer, J., Kimura, J., Hussmann, H., Demartin, B. & Brown, J. M. (2007). Hydrothermal systems in small ocean planets. *Astrobiology* **7**, 987–1005. doi:10.1089/ast.2007.0075.
- Vance, S. D., Hand, K. P. & Pappalardo, R. T. (2016). Geophysical controls of chemical disequilibria in Europa. *Geophysical Research Letters* **43**, 4871–4879. doi:10.1002/2016GL068547.
- van Keken, P. E., Wada, I., Sime, N. & Abers, G. A. (2019). Thermal structure of the forearc in subduction zones: a comparison of methodologies. *Geochemistry, Geophysics, Geosystems* **20**, 3268–3288. doi:10.1029/2019GC008334.
- Winter, J. D. (2010). *An Introduction to Igneous and Metamorphic Petrology*. London: Pearson.
- Wolery, T. J. & Jove-Colon, C. F. (2004). *Qualification of thermodynamic data for geochemical modeling of mineral-water interactions in dilute systems*. Washington, DC: US Department of Energy. doi:10.2172/850412
- Yamada, C., Tsujimori, T., Chang, Q. & Kimura, J.-I. (2019). Boron isotope variations of Franciscan serpentinites, northern California. *Lithos* **334–335**, 180–110. <http://doi.org/10.1016/j.lithos.2019.02.004>
- Zimmer, K., Zhang, Y., Lu, P., Chen, Y., Zhang, G., Dalkilic, M. & Zhu, C. (2016). SUPCRTBL: A revised and extended thermodynamic dataset and software package of SUPCRT92. *Computers & Geosciences* **90**, 97–111. doi:10.1016/j.cageo.2016.02.013.